PERGAMON

International Journal of Solids and Structures 39 (2002) 1275–1305

INTERNATIONAL JOURNAL OF SOLIDS and STRUCTURES

www.elsevier.com/locate/ijsolstr

A thermomechanical model for a 1-D shape memory alloy wire with propagating instabilities

John A. Shaw *

Department of Aerospace Engineering, College of Engineering, The University of Michigan, Francois-Xavier Bagnoud Building, 1320 Beal Avenue, Ann Arbor, MI 48109-2140, USA

Received 22 January 2001

Abstract

A thermomechanical boundary value problem and constitutive model are presented for a shape memory alloy (SMA) wire under uniaxial loading. The intent is to develop a one-dimensional continuum model of an SMA element that includes all the relevant thermomechanical couplings and is suitable for inclusion in finite element analyses. Thermodynamic relations are derived from phenomenological considerations consistent with recent experimental observations and are calibrated to a typical commercially available NiTi wire material. The model includes both temperature-induced and stress-induced transformations that are necessary to exhibit the *shape memory effect* and *pseudoelastic* behaviors. The model accommodates possible unstable mechanical behavior during stress-induced transformations by allowing softening transformation paths and including strain gradient effects. This should provide a tool to study propagating transformation fronts and localized latent heat transfer with the surroundings and a variety of interesting future structural applications, such as composites with embedded SMA elements.

Keywords: Shape memory alloy; Thermomechanical model; Gradient effects; Propagating transformation fronts

1. Introduction

Shape memory alloys (SMAs), such as NiTi-based alloys, exhibit two remarkable properties, the shape memory effect and pseudoelasticity. The shape memory effect is the material's ability to recover large mechanically-induced strains (up to 8%) by moderate increases in temperature (say 20 °C). Pseudoelasticity refers to the ability of the material in a somewhat higher temperature regime to accommodate strains of this magnitude during loading and then recover upon unloading (via a hysteresis loop). The underlying mechanism is a reversible martensitic transformation between solid-state phases, often occurring near room temperature. The transformation can be induced by changes in temperature or by changes in stress due to the strong thermomechanical coupling in the material behavior. The material also has very non-linear mechanical behavior, high internal damping, and high yield stresses. These properties make it an attractive

* Tel.: +1-734-764-3395; fax: +1-734-763-0578.
E-mail address: jashaw@engin.umich.edu (J.A. Shaw).

0020-7683/02/$ - see front matter
PII: S0020-7683(01)00242-6

Nomenclature

Variable	Description
x, X	current and reference axial positions
t	time
τ	characteristic time
l, L	current and reference wire lengths
d, D	current and reference wire diameters
a, A	current and reference cross-section areas
p, P	current and reference cross-section perimeters
ρ, ρ_0	current and reference mass densities
J	determinate of deformation gradient
u	axial displacement
λ	axial stretch ratio
ε	nominal axial strain
σ, Σ	true and nominal axial stresses
t, T	true and nominal tractions
N	axial force
f, F	current and reference axial distributed forces
e	specific internal energy
ϕ	specific Helmholtz free energy
s	specific entropy
c	specific heat
ξ_i	mass fraction of phase i
μ_i	specific chemical force of phase i
θ	absolute wire temperature
θ_a	ambient (bath) temperature
q_x, Q_X	current and reference axial heat fluxes
q_r, Q_R	current and reference radial heat fluxes
k, K	current and reference thermal conductivities
h, H	current and reference film coefficients
E	elastic modulus
β	stress–free transformation strain
α	thermal expansion coefficient
Bi	Biot number

choice for innovative structural applications (see, for example, Duerig et al., 1990; Otsuka and Wayman, 1998).

NiTi's remarkable behavior arises from the interplay of a high temperature phase (austenite), having a cubic atomic lattice structure, and a low temperature phase (martensite), having a monoclinic structure (Otsuka et al., 1971). Fig. 1 shows a differential scanning calorimetry thermogram of a typical commercially available NiTi SMA. The heat input is measured as the temperature of a stress-free sample is changed at a constant rate. The area within the measured peaks and valleys represent the latent heat of transformation between solid-state phases. Due to its low degree of symmetry, the martensite phase exists either as a randomly twinned structure (low temperature, low stress state) or a stress-induced detwinned structure that can accommodate relatively large, reversible strains. Fig. 2 shows the thermomechanical response of a wire

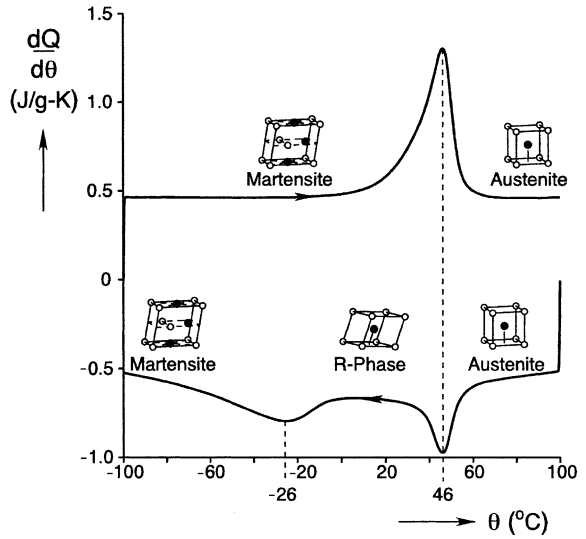

Fig. 1. Differential Scanning Calorimetry of NiTi wire. [Data taken on wire supplied by Memry Corp. used in Shaw and Kyriakides (1995).]

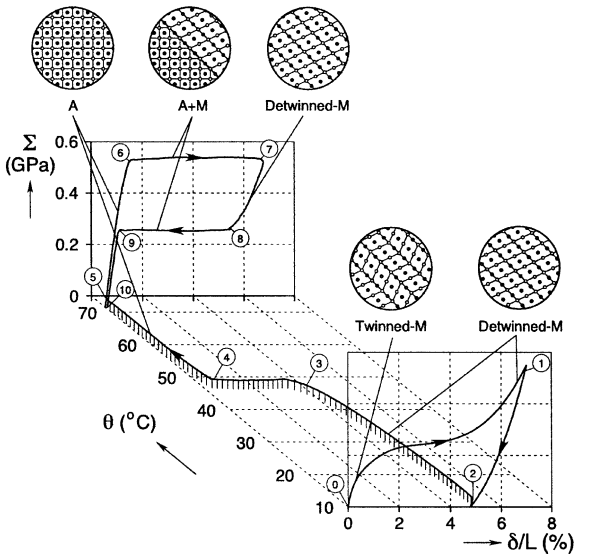

Fig. 2. Thermomechanical behavior of NiTi wire: shape memory effect (⓪ to ④), pseudoelastic loop (⑤ to ⑩). [Data taken on wire supplied by Memry Corp. used in Shaw and Kyriakides (1995). Material has first been quenched in liquid nitrogen to minimize the appearance of the R-phase.]

specimen of the alloy used in Fig. 1 that was tested in a temperature-controlled water bath. The specimen is first subjected to a displacement-controlled load/unload cycle at a relatively low temperature (⓪ to ② in the figure), leaving a 5% apparent permanent strain. The material starts in a twinned martensite (M) state and becomes detwinned upon loading. The specimen is then subjected to a temperature increase while holding the load at a small positive value (② to ⑤). The shape memory effect is seen as the strain is recovered

between points ③ and ④ when the material transforms to austenite (A). The temperature is then held at a relatively high value and the specimen is again subjected to a load/unload cycle under displacement control (⑤ to ⑩). The material undergoes an increase in strain from about 1% to 7% at constant load (⑥ to ⑦) during stretching which is reversed at a lower constant load (⑧ to ⑨) during subsequent unloading (pseudoelastic behavior). In this case the material transforms from austenite to detwinned martensite during loading and then back to austenite during unloading.

The unique properties of equiatomic NiTi were discovered four decades ago (Buehler et al., 1963), and the materials science literature is rich on the subject of the microlevel mechanisms responsible for its unusual behavior. The development of constitutive models appropriate for design studies has been hampered by the complexity of the material behavior and the somewhat limited experimental basis for many years. Bridging the gap between microscopic structure and a macroscopic constitutive model is a complex task and constitutes an area of intensive research (see, for example, Ball and James, 1987; Batthacharya and Kohn, 1996; Siredey et al., 1999). The last decade has seen a variety of constitutive modeling efforts (see, for example, Tanaka et al., 1986; Brinson, 1993; Abeyaratne and Knowles, 1993; Truskinovsky, 1993; Sun and Hwang, 1993; Levitas, 1994; Boyd and Lagoudas, 1994; Patoor et al., 1995; Siredey et al., 1999) including purely phenomenological approaches, plasticity analogues, thermodynamically based continuum models, and detailed micromechanical models. In addition, some notable experimental findings involving temperature and rate sensitivities, unstable behavior, propagating phase transitions, and tension-compression asymmetry effects (see Leo et al., 1993; Shaw and Kyriakides, 1995; Sittner et al., 1995; Gall et al., 1999; Zhang et al., 2000), have provided a better understanding of the material behavior.

Propagating phase transformation phenomena that have been observed in uniaxial pseudoelastic NiTi are particularly interesting features (see, for example, Shaw and Kyriakides, 1997; Sun et al., 2000). Atomic lattice-level instabilities can, in some cases, percolate all the way up to the macroscale, causing mechanical instability, sudden dynamic nucleation events, and then transformation by propagating phase fronts (see Elliott et al., 2001, for a first attempt at lattice-scale modeling). These phenomena cause complex interactions with the surroundings and sometimes surprising rate effects in the material behavior due to latent heat exchanges with the surroundings. Furthermore, similar Lüders-like behavior has been observed during the martensite detwinning response (Liu et al., 1998) of some NiTi alloys (although not the one shown in Fig. 2).

Many applications use SMAs in wire form, since it is generally the least expensive and most readily available form. The distinctly non-uniform strain and temperature fields that occur have important implications on the performance, reliability, and controllability of practical devices. The 1-D thermodynamic framework of Abeyaratne and Knowles (1993) and Knowles (1999) acknowledged such unstable behavior by treating propagating phase boundaries as traveling field discontinuities with appropriate jump conditions. The related work of Abeyaratne et al. (1996), Truskinovsky and Zanzotto (1996), Vainchtein (1999), and Ngan and Truskinovsky (1999) provided analyses of the origins of the pseudoelastic hysteresis arising from the fine microstructural scale. While most current models that treat phase boundary motion do not have any length scale associated with nucleation events or propagating fronts, Sun and Zhong (2000) provided an interesting analysis of the origins of the length scale of nucleation events in an axisymmetric wire arising from the radial strain mismatch between phases.

An alternate approach was demonstrated in Shaw and Kyriakides (1998) for isothermal behavior, and Shaw (2000) and Iadicola and Shaw (in preparation) for coupled thermomechanical behavior. These finite element simulations captured the evolution of propagating transformation fronts and the associated non-uniform temperature and mechanical fields without treating phase fronts as discontinuous quantities. The approach modeled the macroscopic deformation fields during unstable stress-induced transformation in uniaxially loaded thin polycrystalline NiTi specimens with 3-D continuum-level plasticity with a non-monotonic flow rule. The number and speed of propagating fronts was not specified a priori; rather, they were determined naturally by the coupled solution of mechanical equilibrium and the heat equation. The

boundary value problem, however, was not always elliptic in its spatial variables and care was needed to avoid potential pathological mesh sensitivity. Additionally, the plasticity model applicability was limited to irreversible behavior, capturing the stress-induced transformations during loading only (A $\rightarrow$ detwinned M), and the finite element analyses were computationally intensive due to the 3-D approach.

In this paper, a thermomechanical boundary value problem is defined and a new SMA model for a uniaxially loaded, thin SMA wire is presented. The objective is to develop a reduced-dimensional model suitable for finite element implementation. The constitutive model includes reversible stress-induced transformation and temperature-induced transformation necessary to exhibit both the shape memory effect and pseudoelasticity. It is intended to represent thermoelastic behavior within a restricted temperature range centered around the martensitic transformation temperatures (such as the 200 °C range of Fig. 1). The behavior at very high temperatures for which diffusional effects occur, such as annealing, are outside the scope intended here. The model is also intended to be used for stresses up to intermediate values (such as the range shown in Fig. 2). Plasticity effects, which occur at higher stresses, that degrade the shape memory recovery behavior (for example, pseudoelastic loops at high temperatures that do not close) and certain cyclic phenomena involving transformation softening (see Shaw, 1997) are outside the scope of the current work.

Special attention is paid to regimes where transformation occurs in a mechanically unstable manner. The approach is akin to that of Abeyaratne and Knowles (1993), involving the derivation of a free energy function and phase transformation kinetic law, but with gradient effects (see Truskinovsky, 1993). The approach differs, however, in the form of the chosen free energy and the choice of internal field variables (to capture both stress-induced and temperature-induced transformations). Strain gradient effects in the free energy eliminate the possibility of discontinuous strain fields. In this way nucleation events at the macroscale, i.e. strain localization, arise naturally from the solution of the boundary value problem. The model sets the length scale for nucleation and propagating fronts based on a strain gradient energy (an indirect measure of the compatibility effects modeled in Sun and Zhong, 2000). The strength of the gradient term can be calibrated to give any length scale one wishes, either based on experimental observation or dimensional analysis. The model is being implemented in a finite element computer program and solution of structural and design problems using the model will be the subject of forthcoming publications.

The coupled thermomechanical boundary value problem of interest is developed in Section 2, and constitutive restrictions arising from the entropy inequality are given in Section 3. In Section 4, a specific Helmholtz free energy and kinetic relations are developed. The axial pointwise constitutive behavior of the model and predicted calorimetry results, calibrated to some NiTi experiments, are then demonstrated in Section 5. Lastly, Section 6 provides two finite element simulations in a simplified setting in order to demonstrate the ability to model propagating strain fields.

2. Conservation laws

In this section a derivation of the governing field equations is provided using the balance laws of thermodynamics. While the theory is now well established (see, for example, Truskinovsky, 1993; Ngan and Truskinovsky, 1999), the application of fundamental balance laws in this context (thermomechanical coupling and finite deformation with gradient effects for a fine grained, polycrystalline, SMA wire undergoing both stress-induced and temperature-induced transformations) is included here for completeness and clarity of presentation.

The boundary value problem consists of an axisymmetric SMA wire loaded uniaxially and embedded in a medium, either fluid or solid. If the medium is a fluid it acts as a thermal bath with a (possibly) time varying ambient temperature, $\theta_a(t)$. If the medium is a solid it transmits heat and mechanical loads to the SMA wire. The initial geometry of the wire is described by its reference length, L, and cross-sectional area,

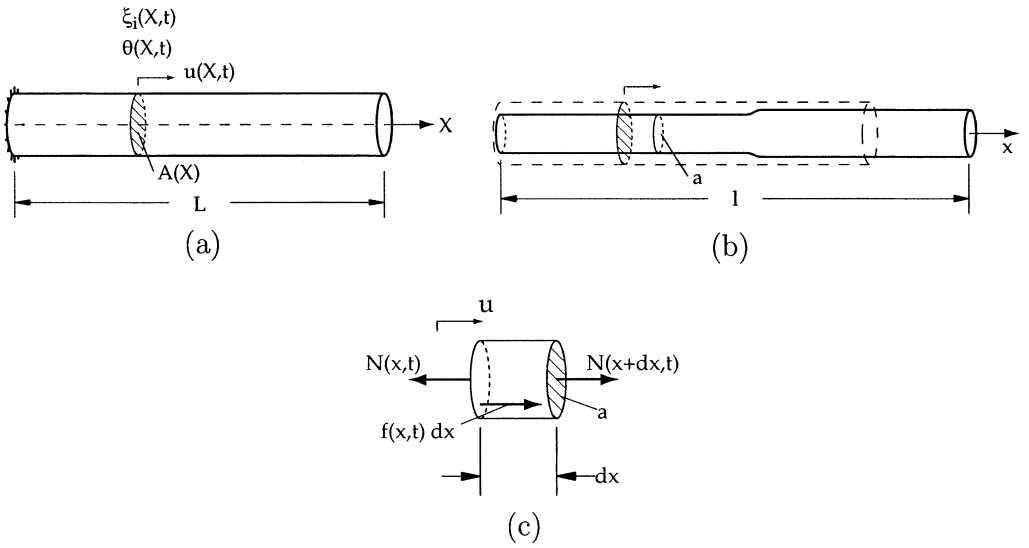

Fig. 3. (a) Reference configuration, (b) current configuration showing propagating neck (transformation front), (c) free body diagram of infinitesimal section.

A (see Fig. 3a). To justify the 1-D context the area of the wire, $A(X)$, is assumed to be slowly varying. The relevant fields, displacement $u(X,t)$, absolute temperature $\theta(X,t)$, and internal variables $\xi_i(X,t)$, are functions of one spatial dimension, X (reference position), and time, t.

2.1. Conservation of mass

Conservation of mass between the reference configuration and current configuration is

$$\rho_0 A\,\mathrm{d}X = \rho a\,\mathrm{d}x, \tag{1}$$

where x is the material coordinate in the current configuration (see Fig. 3b), and a is the current cross-sectional area. Throughout this paper, uppercase and lowercase versions of the same variable refer to reference and current configuration quantities, respectively. Using the axial stretch ratio, $\lambda = \mathrm{d}x/\mathrm{d}X$, and the ratio of the reference and current mass densities, $J \equiv \rho_0/\rho$, we get

$$JA = a\lambda. \tag{2}$$

Furthermore, martensitic transformations can often be considered nearly isochoric ($\rho_0 = \rho$), so the following is assumed from here on.

$$J = 1, \qquad A = a\lambda. \tag{3}$$

2.2. Conservation of linear momentum

Conservation of linear momentum in the current configuration can be expressed as

$$\frac{\mathrm{d}}{\mathrm{d}t}\int_{x_1}^{x_2} \dot{\boldsymbol{u}}\rho a\,\mathrm{d}x = [N]_{x_1}^{x_2} + \int_{x_1}^{x_2} f\,\mathrm{d}x. \tag{4}$$

where N is the tensile force in the wire, $\dot{\boldsymbol{u}} = \partial u(X,t)/\partial t$ is the material velocity, and the notation $[N]_{x_1}^{x_2}$ represents $N(x_2,t) - N(x_1,t)$. Using mass conservation, the divergence theorem and the arbitrariness of the

interval $[x_1, x_2]$ (or the free body diagram, Fig. 3c), the equation of motion of a 1-D structural element subjected to an axial distributed load, f (force/current length), is

$$N_{,x} + f = \rho a \ddot{u}, \tag{5}$$

where $N_{,x}$ refers to $\partial N/\partial x$. It is equivalently expressed in the reference configuration, using Eqs. (1) and (2), as

$$N' + F = \rho_0 A \ddot{u}, \tag{6}$$

where N' refers to $\partial N/\partial X$, and $F \equiv f\lambda$ is the distributed force per unit reference length.

The application of the divergence theorem is justified provided the field quantities are sufficiently smooth (otherwise, jump conditions must be specified across surfaces which exhibit discontinuities as in Abeyaratne and Knowles, 1993). One of the objectives of the current formulation is to ensure all field quantities remain sufficiently smooth. Anticipating the possibility of non-monotonic stress–strain behavior with an intermediate softening branch, multiple strain states are possible for a given stress value. In a 1-D framework this admits the possibility of discontinuous strain fields under equilibrium conditions. Instead, we seek to ensure that unstable mechanical behavior gives rise to localized, but smooth, deformation of the type shown in Fig. 3b. A non-local constitutive relation for stress is needed, which necessarily introduces a length scale into the constitutive model. In this case, the length scale of interest is the wire diameter, since the axial extent of a local propagating neck (or transformation front) is expected to be of this size. We presume that the wire is polycrystalline with a sufficient number of grains such that compatibility is the dominant consideration in regions with strong strain gradients.

A strain gradient approach, therefore, is used to account for off-axis effects in a 1-D framework (similar justification and approach to that of Coleman (1983) for drawing of polymeric fibers). It is well known that such a gradient approach avoids the singularity in the equilibrium equation (loss of ellipticity in the multidimensional case) as the local tangent modulus changes sign. It also avoids the possibility of discontinuous strain fields that could lead to pathological mesh dependence in a finite element implementation. For a review of strain gradient theories see the article by Fleck and Hutchinson (1996). The approach first proposed by Mindlin (1965) and generalized to finite deformation kinematics as in Leroy and Molinari (1993), is adopted. Specializing to one-dimension, the generalized principle of virtual work can be written as

$$\int_{x_1}^{x_2} \left(\overset{1}{\sigma}\delta\tilde{\varepsilon} + \overset{2}{\sigma}\delta\tilde{\varepsilon}_{,x} \right) a \,\mathrm{d}x = \int_{x_1}^{x_2} (f - \rho a\ddot{u})\delta u \,\mathrm{d}x + \left[\overset{1}{t} a \delta u \right]_{x_1}^{x_2} + \left[\overset{2}{t} a \delta u_{,x} \right]_{x_1}^{x_2}, \tag{7}$$

where $\overset{1}{\sigma}$ and $\overset{2}{\sigma}$ are the Cauchy-like (or true) axial stresses conjugate to the virtual strain $\delta\tilde{\varepsilon}$ and virtual strain gradient $\delta\tilde{\varepsilon}_{,x}$, respectively, $\overset{1}{t}$ and $\overset{2}{t}$ are the end tractions conjugate to the virtual displacement δu and virtual displacement gradient $\delta u_{,x}$, respectively. Alternatively, the left hand side of Eq. (7) can be transformed to the reference configuration, thereby inducing the following equivalent statement,

$$\int_{X_1}^{X_2} \left(\overset{1}{\Sigma}\delta\lambda + \overset{2}{\Sigma}\delta\lambda' \right) A \,\mathrm{d}X = \int_{X_1}^{X_2} (F - \rho_0 A\ddot{u})\delta u \,\mathrm{d}X + \left[\overset{1}{T} A \delta u \right]_{X_1}^{X_2} + \left[\overset{2}{T} A \delta u' \right]_{X_1}^{X_2}, \tag{8}$$

where $\overset{1}{\Sigma}$ and $\overset{2}{\Sigma}$ are the nominal-like (first Piola–Kirchhoff) stresses conjugate to the stretch, and its gradient, respectively, and $\overset{1}{T}$ and $\overset{2}{T}$ are the referential end tractions. Integrating the left hand side of Eq. (8) by parts gives

$$\int_{X_1}^{X_2} \left[-\left(A\overset{1}{\Sigma} \right)' + \left(A\overset{2}{\Sigma} \right)'' \right] \delta u \,\mathrm{d}X + \left[\left(A\overset{1}{\Sigma} - \left(A\overset{2}{\Sigma} \right)' \right) \delta u \right]_{X_1}^{X_2} + \left[A\overset{2}{\Sigma}\delta u' \right]_{X_1}^{X_2}. \tag{9}$$

Combining Eqs. (8) and (9) an invoking the arbitrariness of δu produces the same governing equation as (6), but with the axial force now interpreted as

$$N = \overset{1}{\Sigma} A - \left(\overset{2}{\Sigma} A \right)' \tag{10}$$

and boundary condition as

$$\overset{1}{T} A = \overset{1}{\Sigma} A - \left(\overset{2}{\Sigma} A \right)' \quad \text{and} \quad \overset{2}{T} = \overset{2}{\Sigma}. \tag{11}$$

At the ends $X = 0, L$ the gradient traction, $\overset{2}{T}$, is often set to zero, thereby providing the necessary higher order boundary condition. Note also that deriving the governing differential equation in the current configuration provides relations between Cauchy and nominal-like stresses,

$$\begin{aligned} \overset{1}{\Sigma} &= \lambda^{-1} \overset{1}{\sigma}, \\ \overset{2}{\Sigma} &= \lambda^{-2} \overset{2}{\sigma}. \end{aligned} \tag{12}$$

2.3. Conservation of energy

The heat equation for the wire is derived from the first law of thermodynamics (or energy conversation). The rate of increase of internal energy and kinetic energy is equal to the rate at which thermal and mechanical energy is supplied to the wire. This can be expressed in the current configuration as

$$\frac{\mathrm{d}}{\mathrm{d}t} \left[\int_{x_1}^{x_2} e \rho a \, \mathrm{d}x + \int_{x_1}^{x_2} \frac{1}{2} \dot{\boldsymbol{u}}^2 \rho a \, \mathrm{d}x \right] = -[q_x a]_{x_1}^{x_2} - \int_{x_1}^{x_2} q_r p \, \mathrm{d}x + \left[\overset{1}{t} a \dot{\boldsymbol{u}} \right]_{x_1}^{x_2} + \left[\overset{2}{t} a \dot{\boldsymbol{u}}_{,x} \right]_{x_1}^{x_2} + \int_{x_1}^{x_2} f \dot{\boldsymbol{u}} \, \mathrm{d}x, \tag{13}$$

where e is the specific internal energy, q_x is the axial heat flux, q_r is the radial heat flux, and p is the current circumference (perimeter) of the wire. Using the relations between reference and current heat flux quantities

$$Q_X A = q_x a \quad \text{or} \quad Q_X = q_x / \lambda, \tag{14}$$

$$Q_R P \, \mathrm{d}X = q_r p \, \mathrm{d}x \quad \text{or} \quad Q_R = q_r \sqrt{\lambda}, \tag{15}$$

allows energy conservation to be written in the reference configuration as

$$\begin{aligned} \frac{\mathrm{d}}{\mathrm{d}t} \left[\int_{X_1}^{X_2} e \rho_0 A \, \mathrm{d}X + \int_{X_1}^{X_2} \frac{1}{2} \dot{\boldsymbol{u}}^2 \rho_0 A \, \mathrm{d}X \right] &= -[Q_X A]_{X_1}^{X_2} - \int_{X_1}^{X_2} Q_R P \, \mathrm{d}X + \left[\overset{1}{T} A \dot{\boldsymbol{u}} \right]_{X_1}^{X_2} + \left[\overset{2}{T} A \dot{\boldsymbol{u}}' \right]_{X_1}^{X_2} \\ &\quad + \int_{X_1}^{X_2} F \dot{\boldsymbol{u}} \, \mathrm{d}X. \end{aligned} \tag{16}$$

The divergence theorem gives

$$\int_{X_1}^{X_2} (\dot{e} + \ddot{\boldsymbol{u}} \dot{\boldsymbol{u}}) \rho_0 A \, \mathrm{d}X = -\int_{X_1}^{X_2} [(Q_X A)' + Q_R P] \, \mathrm{d}X + \int_{X_1}^{X_2} \left[(N \dot{\boldsymbol{u}})' + \left(\overset{2}{\Sigma} A \dot{\boldsymbol{u}}' \right)' + F \dot{\boldsymbol{u}} \right] \mathrm{d}X. \tag{17}$$

Using Eqs. (6) and (10) and invoking the arbitrariness of X_1 and X_2, the heat equation in the reference configuration is

$$\rho_0 A \dot{e} = -(Q_X A)' - Q_R P + \overset{1}{\Sigma} A \dot{\boldsymbol{\lambda}} + \overset{2}{\Sigma} A \dot{\boldsymbol{\lambda}}'. \tag{18}$$

A simple model for the radial heat flux is

$$Q_R = -H(\theta - \theta_\mathrm{a}), \tag{19}$$

where H is the referential film coefficient, θ is the wire temperature, and θ_a is the ambient temperature. Note that due to Eqs. (3) and (15) the film coefficient in the current and reference configurations are related by $H = h\sqrt{\lambda}$. Consistent with the 1-D assumption, the gradient of the temperature across the wire in the radial direction is assumed to be negligible. This is true if the surrounding medium is much less conductive than the wire. In particular, the Biot number Bi, the non-dimensional ratio of the radial thermal resistance to the boundary thermal resistance, should be much less than unity (Incropera and DeWitt, 1996). That is,

$$Bi \equiv HR/K \ll 1, \tag{20}$$

where R is the wire radius. For an air medium the dominant heat transfer mechanism is convection. A typical NiTi wire in stagnant air with $K = 18$ W/Km, $H = 4$ W/Km^2, and $R = 0.4$ mm, has a Biot number of the order of 10^{-4}; therefore, the radial temperature gradient can reasonably be neglected.

3. Restrictions on constitutive relations

The second law of thermodynamics is satisfied by adopting the approach of Coleman and Noll (1963) and Coleman and Gurtin (1967), where restrictions are placed on the constitutive relations. The total change in entropy of the wire and its surroundings must be non-negative,

$$\frac{\mathrm{d}}{\mathrm{d}t}\int_{x_1}^{x_2} s\rho a\,\mathrm{d}x + \left[\frac{q_x a}{\theta}\right]_{x_1}^{x_2} + \int_{x_1}^{x_2} \frac{q_r p}{\theta}\,\mathrm{d}x \geqslant 0, \tag{21}$$

where s is the specific entropy of the wire. Using the divergence theorem once again we obtain

$$\int_{x_1}^{x_2} \left[\dot{s}\rho a + \left(\frac{q_x a}{\theta}\right)_{,x} + \frac{q_r p}{\theta}\right]\mathrm{d}x \geqslant 0, \tag{22}$$

which is an integral form of the Clausius–Duhem inequality for arbitrary interval $[x_1, x_2]$. Converting to the reference configuration, the entropy inequality becomes

$$\int_{X_1}^{X_2} \left[\dot{s}\rho_0 A + \left(\frac{Q_X A}{\theta}\right)' + \frac{Q_R P}{\theta}\right]\mathrm{d}X \geqslant 0. \tag{23}$$

Eliminating the divergence of the heat flux by using the heat equation (18) the entropy production rate becomes

$$\int_{X_1}^{X_2} \left[\rho_0 A(\theta\dot{s} - \dot{e}) - \frac{\theta'}{\theta} Q_X A + \overset{1}{\Sigma} A\dot{\lambda} + \overset{2}{\Sigma} A\dot{\lambda}'\right]\frac{\mathrm{d}X}{\theta} \geqslant 0. \tag{24}$$

The behavior of the wire is determined from knowledge of the following field quantities: the displacement field $u(X,t)$, the temperature field $\theta(X,t)$, and phase fraction fields $\xi_1(X,t)$, $\xi_2(X,t)$, and $\xi_3(X,t)$ as discussed below. Each of these is a function of axial position X and time t. Since axial position is the only spatial variable all quantities are interpreted to be average quantities across the cross-section of the wire.

As discussed previously the underlying mechanism for shape memory behavior is a change in crystal structure from a high symmetry lattice (austenite—often cubic) to a low symmetry lattice (martensite—monoclinic in the case of NiTi) upon cooling. Martensite has several energetically equivalent variants, which are simple rotations or reflections of the crystal structure. If little or no macroscopic stress exists during the transformation from A to M the microstructure will be randomly twinned, resulting in no change in macroscopic strain. If a sufficient stress, however, is applied the structure will become detwinned, resulting in the reorientation of some variants into other variants that are preferentially aligned with the applied stress. The number of martensite variants can be large (24 in the case of NiTi), but only those that

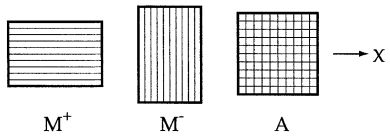

Fig. 4. Three uniaxial phases: two variants of martensite and austenite.

contribute to axial stretching or shortening are relevant here (see Fig. 4). Therefore, ξ_1 represents the phase fraction of martensite that contributes to axial stretching (M^+); ξ_2 represents the phase fraction of martensite that contributes to axial shortening (M^-); and ξ_3 represents the phase fraction of austenite (A). Equal fractions of ξ_1 and ξ_2 represents a twinned microstructure. These three phase fractions (ξ_1, ξ_2, ξ_3) are necessary to model the shape memory effect, in which the material transforms from austenite $(0, 0, 1)$ to twinned martensite $(\frac{1}{2}, \frac{1}{2}, 0)$ upon cooling, then to detwinned martensite $(1, 0, 0)$ upon loading–unloading, then back to austenite upon heating (see the thermomechanical cycle ④, ⓪, to ④ in Fig. 2).

Accordingly, this is a mixture theory where more than one phase can be present at a given axial position along the wire. The phase fractions are interpreted as mass fractions (actually they can also be termed volume fractions in this context since transformations are assumed to be isochoric). They are subject to mass conservation constraints

$$\xi_1 + \xi_2 + \xi_3 = 1 \quad \text{and} \quad \xi_i \geqslant 0 \quad \text{for} \quad i = 1, 2, 3. \tag{25}$$

Pictorially, phase fractions are free to wander within the triangular planar region shown in Fig. 5. Consequently, only two phase fractions are independent, and we choose to use ξ_1 (M^+ fraction) and ξ_2 (M^- fraction). No other explicit compatibility requirements are enforced between phases at the microscale (other than indirectly through the strain gradient penalty), since such microstructural details are below the scale of interest. The exact distribution of phases within the wire cross-section is unknown and one could envision various possibilities as shown in Fig. 6. Nevertheless, the two phase fractions can vary independently, and their effect is to alter the average properties of the cross-section, i.e., the effective properties along the X-axis.

The constitutive relations for an SMA element are based on a specific Helmholtz free energy, $\phi(\lambda, \lambda', \theta, \xi_1, \xi_2)$. Using the definition of the Helmholtz free energy, $(\phi \equiv e - \theta s)$, Eq. (24), and grouping rate terms, the entropy production becomes

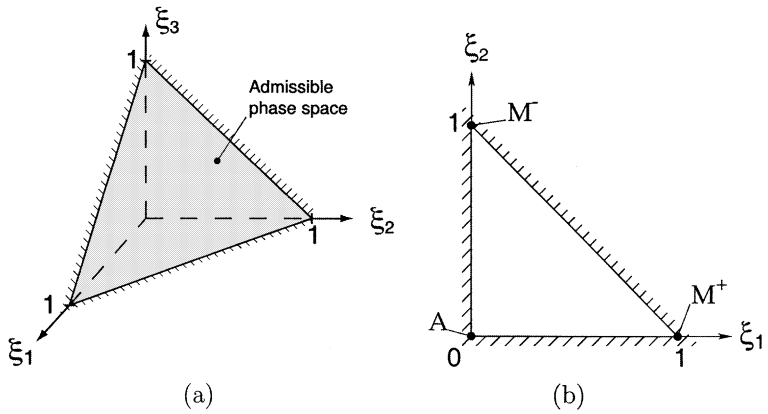

Fig. 5. Admissible phase space, (a) 3-D plane, (b) 2-D projection.

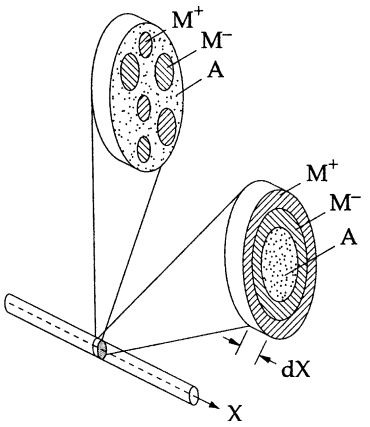

Fig. 6. Possible distributions of phases within the cross-section of wire.

$$\int_{X_1}^{X_2}\left[-\rho_0 A(\phi_{,\theta}+s)\dot{\theta}+\left(\overset{1}{\Sigma}A-\rho_0 A\phi_{,\lambda}\right)\dot{\lambda}+\left(\overset{2}{\Sigma}A-\rho_0 A\phi_{,\lambda'}\right)\dot{\lambda}'-\rho_0 A\phi_{,\xi_i}\dot{\xi}_i-\frac{1}{\theta}Q_X\theta'\right]\frac{\mathrm{d}X}{\theta}\geqslant 0. \tag{26}$$

The arbitrariness of the interval $[X_1, X_2]$, of $\dot{\theta}$, $\dot{\lambda}$, and $\dot{\lambda}'$, and the non-negativity requirement lead to the following Gibb's relations

$$\begin{aligned} s &= -\phi_{,\theta},\\ \overset{1}{\Sigma} &= \rho_0\phi_{,\lambda},\\ \overset{2}{\Sigma} &= \rho_0\phi_{,\lambda'}. \end{aligned} \tag{27}$$

Entropy production arises, therefore, only from the phase transformation and heat flux terms, and so we require

$$\begin{aligned} \mu_i\dot{\xi}_i &\geqslant 0,\\ -Q_X\theta' &\geqslant 0, \end{aligned} \tag{28}$$

where the chemical driving forces (relative to austenite) are defined as $\mu_i \equiv -\phi_{,\xi_i}$ $(i=1,2)$. The heat flux inequality (28) is satisfied, if we assume the conventional axial heat conduction law

$$Q_X = -K\theta', \tag{29}$$

where K is a positive (referential) thermal conductivity for the material. (Using $q_x = -k\theta_{,x}$, Eqs. (3) and (15), results in the relation between the current and reference conductivities $k = \lambda^2 K$.) The conductivity is assumed to follow the linear mixture rule,

$$K(\xi_1,\xi_2) = K_{\mathrm{A}} + (\xi_1+\xi_2)\,\Delta K, \tag{30}$$

where K_{A} is the thermal conductivity of pure austenite, and $\Delta K = K_{\mathrm{M}} - K_{\mathrm{A}}$ is the difference in conductivity between martensite and austenite. It is known, for example, that the thermal conductivity can change by a factor of two depending on the phase (Faulkner et al., 2000).

Using the definition of Helmholtz free energy, the Gibb's relations (27), and the heat flux constitutive relations (19) and (29), the heat equation is now written as

$$\rho_0 A\dot{Q}_{\mathrm{s}} = (KA\theta')' + HP(\theta-\theta_{\mathrm{a}}), \tag{31}$$

where $\dot{Q}_{\mathrm{s}}$ is the specific heat storage rate defined as

$$\dot{Q}_s \equiv \theta \dot{s} - \mu_i \dot{\xi}_i, \tag{32}$$

and summation is implied on the repeated index i from 1 to 2. In general the entropy of the material can have the same functional dependence as the Helmholtz free energy, $s = s(\lambda, \lambda', \theta, \xi_1, \xi_2)$, so the rate of change is

$$\dot{s} = s_{,\lambda}\dot{\lambda} + s_{,\lambda'}\dot{\lambda}' + s_{,\theta}\dot{\theta} + s_{,\xi_i}\dot{\xi}_i. \tag{33}$$

The first derivatives of entropy are related to the second derivatives of the Helmholtz free energy and can be interpreted as

$$\begin{aligned} \rho_0 s_{,\lambda} &= -\overset{1}{\Sigma}_{,\theta}, \\ \rho_0 s_{,\lambda'} &= -\overset{2}{\Sigma}_{,\theta}, \\ s_{,\theta} &= \frac{c}{\theta}, \\ s_{,\xi i} &= \mu_{i,\theta}, \end{aligned} \tag{34}$$

where c is the specific heat of the material. Consequently, the heat storage rate may be written as

$$\rho_0 \dot{Q}_s = -\theta\left(\overset{1}{\Sigma}_{,\theta}\dot{\lambda} + \overset{2}{\Sigma}_{,\theta}\dot{\lambda}'\right) + \rho_0 c\dot{\theta} + \rho_0\left(\theta\mu_{i,\theta} - \mu_i\right)\dot{\xi}_i, \tag{35}$$

where the first two terms represent the thermoelastic and sensible heat change, and the last term represents the latent heat change.

All that remains is to ensure that the kinetic relations

$$\dot{\xi}_i = V_i(\mu_1, \mu_2), \quad i = 1, 2 \tag{36}$$

satisfy Eq. (28) to guarantee a non-negative entropy production. This will be addressed in the Section 4.

4. Constitutive relations

The constitutive behavior of the material is completely determined once the form of the free energy and the kinetic relations are specified. Each of these is addressed in turn in the following two sections.

4.1. Helmholtz free energy

The free energy is decomposed into three parts as

$$\phi(\varepsilon, \varepsilon', \theta, \xi_i) = \phi_E(\varepsilon, \varepsilon', \theta, \xi_i) + \phi_C(\theta, \xi_i) + \phi_T(\theta), \tag{37}$$

where ϕ_E is the specific elastic (or mechanical) strain energy, ϕ_C is the specific chemical free energy, and ϕ_T is the specific phase-independent thermal free energy. The nominal strain, $\varepsilon \equiv \lambda - 1$, will be used from here on. Note that the maximum strain that would be expected for a NiTi SMA is on the order of 0.08, so finite strain kinematics may or may not be necessary, depending on the desired accuracy.

4.1.1. Elastic energy

The elastic strain energy density is chosen as

$$\rho_0\phi_E(\varepsilon, \varepsilon', \theta, \xi_i) = \frac{E(\xi_1, \xi_2)}{2}\left[\varepsilon - (\xi_1 - \xi_2)\beta - \alpha(\xi_1, \xi_2)\,\Delta\theta\right]^2 + \frac{\gamma}{2}\varepsilon'^2, \tag{38}$$

where E is the phase-dependent elastic modulus, β is the transformation strain (a material constant), and α is the phase-dependent thermal expansion coefficient. The expression (38) assumes an additive decomposition of strain that is consistent with a small strain theory. The modulus follows the linear mixture rule

$$E(\xi_1, \xi_2) = E_A + (\xi_1 + \xi_2)\,\Delta E, \tag{39}$$

where E_A is the modulus of pure austenite and $\Delta E = E_M - E_A$ is the difference in martensite to austenite modulus. Note that in the neighborhood of the transformation (say 50 °C on either side of the transformation) the strain due to thermal expansion is two orders of magnitude less than the typical transformation strain, so from here on thermal expansion effects will be neglected. The axial strain field is assumed to be constant within the cross-section and each constituent supports an effective partial stress in the axial direction (see Fig. 6). There is no attempt here to identify a specific microstructure, which would require summing the volumetric energies of individual phases and interfacial energies between phase boundaries. Rather, the interpretation of the internal parameters as actual phase fractions is relaxed somewhat. The aim is to develop an engineering-level model, not to identify mechanisms at a lower length scale (although an interesting problem), so the phase fractions in this context are used as interpolation parameters between the axial elastic stress–strain response of the pure constituents (see Fig. 7). Furthermore, discontinuous axial strain fields are not permitted, so a strain gradient penalty (the term involving ε') is added to the strain energy in Eq. (38). According to the Gibb's relations (27), the first and second order stresses are now

$$\begin{aligned} \overset{1}{\Sigma} &= [E_A + (\xi_1 + \xi_2)\,\Delta E][\varepsilon - (\xi_1 - \xi_2)\beta], \\ \overset{2}{\Sigma} &= \gamma\varepsilon'. \end{aligned} \tag{40}$$

The inclusion of the strain gradient term in the elastic energy is a special case of and is consistent with the approaches of Coleman (1983), which provided a heuristic argument, and Triantafyllidis and Bardenhagen (1993), which derived parameters from an explicit microstructure of non-local spring networks. The material parameter, γ, is the strength of the strain gradient effect and can in general be a function of ε, θ, and ξ_i's, but here we assume it to be a constant for simplicity (and in the absence of clear data to model its dependence). A length scale appears in the energy associated with the strain gradient term $\frac{\gamma}{2}\varepsilon'^2$, since ε' has units of L^{-1}. A nonzero value of γ ensures that transformation fronts, if present, appear as propagating necks (see Fig. 3b), each with a smooth profile. This is consistent with experimental observations of

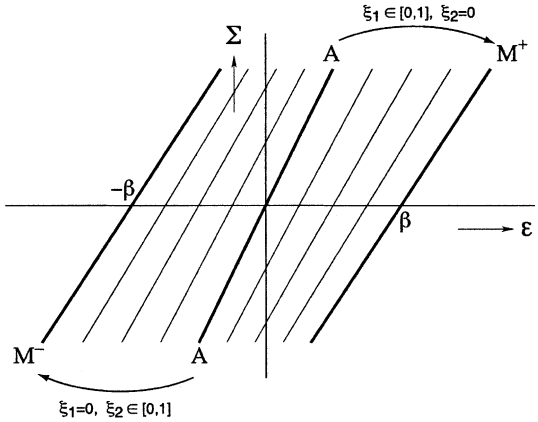

Fig. 7. Interpolation of linear elastic stress–strain responses between pure phases.

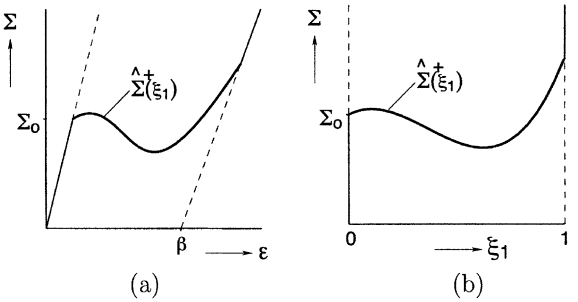

Fig. 8. General $A \rightarrow M^+$ transformation isotherm: (a) stress–strain, (b) stress–phase fraction.

propagating strain fields in fine-grained, polycrystalline wires where the axial extent is of the order of the wire radius. Without this gradient effect discontinuous axial strain fields could appear in the boundary value problem whenever the mechanical behavior becomes unstable.

4.1.2. Chemical and thermal energy

The form of the chemical part of the free energy $\phi_C(\theta, \xi_1, \xi_2)$ is found from assumed mechanical isotherms that capture the nucleation peaks and transformation stresses observed in experiments. Stress-induced phase transformations, $A \rightarrow M^+$ and $A \rightarrow M^-$, are modeled along user-specified trajectories $\hat{\Sigma}^+(\theta, \xi_1)$ and $\hat{\Sigma}^-(\theta, \xi_2)$, respectively, in the stress-phase fraction space (see, for example, Fig. 8).

Consider first the free energy for the $A \rightarrow M^+$ transformation ($\xi_2 = 0$) at a relatively high, constant temperature under homogeneous strain ($\varepsilon' = 0$),

$$\rho_0 \phi(\varepsilon, 0, \theta, \xi_1, 0) = \frac{E_A + \xi_1 \Delta E}{2} (\varepsilon - \xi_1 \beta)^2 + G_1(\theta, \xi_1) + \rho_0 \phi_T(\theta), \tag{41}$$

where $G_1(\theta, \xi_1) \equiv \phi_C(\theta, \xi_1, 0)$. According to the constitutive law, the nominal stress is

$$\rho_0 \left(\frac{\partial \phi}{\partial \varepsilon} \right)^{A \rightarrow M^+} = (E_A + \xi_1 \Delta E)(\varepsilon - \xi_1 \beta) = \hat{\Sigma}^+(\theta, \xi_1), \tag{42}$$

which specifies a parametric relation for the strain, ε, with ξ_1. Along the trajectory the appropriate chemical driving force is set to zero, thereby defining a reversible equilibrium path. (The kinetic relation discussed later will be used to impose any hysteretic behavior.) Therefore, we enforce

$$\rho_0 \left(\frac{\partial \phi}{\partial \xi_1} \right)^{A \rightarrow M^+} = \frac{\Delta E}{2} (\varepsilon - \xi_1 \beta)^2 - \beta (E_A + \xi_1 \Delta E)(\varepsilon - \xi_1 \beta) + \frac{\partial G_1}{\partial \xi_1} = 0. \tag{43}$$

Eliminating the strain using Eq. (42), we get

$$\frac{\partial G_1}{\partial \xi_1} = \beta \hat{\Sigma}^+(\theta, \xi_1) - \frac{\Delta E}{2} \left[\frac{\hat{\Sigma}^+(\theta, \xi_1)}{E_A + \xi_1 \Delta E} \right]^2, \tag{44}$$

which can be integrated to obtain G_1 once $\hat{\Sigma}^+(\theta, \xi_1)$ is known. A similar relation is derived for the $A \rightarrow M^-$ transformation for compressive behavior,

$$\frac{\partial G_2}{\partial \xi_2} = -\beta \hat{\Sigma}^-(\theta, \xi_2) - \frac{\Delta E}{2} \left[\frac{\hat{\Sigma}^-(\theta, \xi_2)}{E_A + \xi_2 \Delta E} \right]^2, \tag{45}$$

where $G_2(\theta, \xi_2) \equiv \phi_C(\theta, 0, \xi_2)$. Integration constants must be chosen such that $G_1(\theta, 0) = G_2(\theta, 0)$.

As an example, one can impose a temperature-dependent, but otherwise constant, tangent modulus, $E_t(\theta) = d\Sigma/d\varepsilon$ for the special case of a linear trajectory in stress–strain space with temperature dependent nucleation strains, $\varepsilon_n(\theta)$ or $-\varepsilon_n(\theta)$, depending on the sign of the stress (see Fig. 9).

$$\begin{aligned}
\Sigma^+ &= E_A\varepsilon_n(\theta) + E_t(\theta)[\varepsilon - \varepsilon_n(\theta)], \quad \text{for} \quad \mu_1 = 0,\ \xi_2 = 0,\ 0 \leqslant \xi_1 \leqslant 1, \\
\Sigma^- &= -E_A\varepsilon_n(\theta) + E_t(\theta)[\varepsilon + \varepsilon_n(\theta)], \quad \text{for} \quad \mu_2 = 0,\ \xi_1 = 0,\ 0 \leqslant \xi_2 \leqslant 1.
\end{aligned} \tag{46}$$

Considering first the $A \rightarrow M^+$ transformation, the solution of the parametric form of the equation,

$$E_t = \frac{\partial\hat{\Sigma}^+/\partial\xi_1}{\partial\varepsilon/\partial\xi_1}, \tag{47}$$

is

$$\hat{\Sigma}^+ = \frac{(E_A + \xi_1\Delta E)[E_t\xi_1\beta - (E_t - E_A)\varepsilon_n]}{E_A + \xi_1\Delta E - E_t}. \tag{48}$$

This is substituted into Eq. (44) and integrated to obtain G_1. The above relations are symmetric with respect to tension and compression, and thus G_1 and G_2 have the same form. This need not be the case in general, since it is well known (Gall et al., 1999) that SMAs with significant crystallographic texture have non-symmetric behavior. Nevertheless, for these chosen transformation paths, we have

$$\begin{aligned}
G_1 = G_2 = G(\theta,\xi) &= A(\theta)\xi + B(\theta)\xi^2 + \frac{C(\theta)}{D(\theta)+\xi} - \frac{C(\theta)}{D(\theta)} \\
A(\theta) &= \frac{[\beta E_t(\theta)]^2}{2\Delta E} + \beta\varepsilon_n(\theta)[E_A - E_t(\theta)] \\
B(\theta) &= \frac{1}{2}\beta^2 E_t(\theta) \\
C(\theta) &= \frac{1}{2\Delta E^3}[\beta E_t(\theta) - \Delta E\varepsilon_n(\theta)]^2[E_A - E_t(\theta)]^2 \\
D(\theta) &= \frac{E_A - E_t(\theta)}{\Delta E}.
\end{aligned} \tag{49}$$

Note that the integration constant in $G(\theta,\xi)$ is chosen so that $G(\theta,0) = 0$ to ensure continuity of the function at $\xi_1 = \xi_2 = 0$. The surface $\phi_C(\theta,\xi_1,\xi_2)$ in ξ_1–ξ_2 space is constructed by assuming the following interpolation.

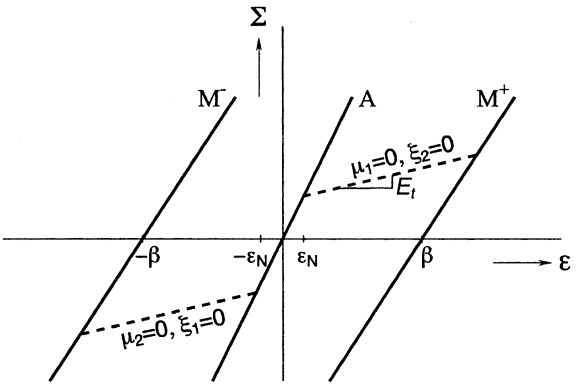

Fig. 9. Linear stress-induced transformation paths.

$$\rho_0\phi_C(\theta,\xi_1,\xi_2) = (1-2\xi_2)G(\theta,\xi_1) + (1-2\xi_1)G(\theta,\xi_2) + 4\xi_1\xi_2\rho_0\phi_{mix}(\theta). \tag{50}$$

In this way the conditions for $\phi_C(\theta,\xi_1,0)$ and $\phi_C(\theta,0,\xi_2)$ are satisfied for stress-induced transformations occurring along the phase space edges, and $\phi_C(\theta,\frac{1}{2},\frac{1}{2}) = \phi_{mix}(\theta)$ represents the free energy of the twinned martensite material. The elastic and chemical parts of the free energy (ϕ_E and ϕ_C) are now completely determined once the material constants, E_A, ΔE, β, and γ, and temperature-dependent functions, $\varepsilon_n(\theta)$, $E_t(\theta)$, and $\phi_{mix}(\theta)$, are specified.

Lastly, integrating the phase-independent part of the specific heat (assumed to be constant) in Eq. (34) and then the entropy in Eq. (27) with respect to temperature, the thermal part of the free energy (ϕ_T) is written as

$$\phi_T(\theta) = \phi_0 - \theta s_0 - c_0\theta[\log(\theta) - 1], \tag{51}$$

where ϕ_0, s_0, and c_0 are material constants representing the temperature-independent and phase-independent free energy, entropy, and specific heat, respectively.

4.2. Kinetic relation

The kinetic relation must satisfy the entropy condition (28). The direction of phase transformation is assumed to be colinear with the gradient of the chemical driving force, except at the boundary of the admissible phase region. In the interior of the phase space the adopted kinetic relation is

$$\dot{\boldsymbol{\xi}} = V(\mu)\boldsymbol{\mu}/\mu, \tag{52}$$

where μ is the magnitude of the chemical force vector and $\boldsymbol{\mu}/\mu$ is the unit vector in the direction of the chemical force. The entropy requirement (28) requires that $V(\mu)$ satisfy $\mu V(\mu) \geqslant 0$. This allows many possible kinetic laws to be adopted. A piecewise linear relationship as in Fig. 10a, for example, is

$$V(\mu) = \begin{cases} v_0(\mu+\mu_c) & : \quad \mu < -\mu_c \\ 0 & : \quad -\mu_c \leqslant \mu \leqslant \mu_c \\ v_0(\mu-\mu_c) & : \quad \mu > \mu_c. \end{cases} \tag{53}$$

The constant μ_c determines the critical chemical force required for the phase transformation to proceed. A non-zero value of μ_c creates a quasi-static hysteresis for the transformation. The material constant v_0 determines the speed of the phase transformation. The speed of transformation in an SMA is usually limited by the rate at which heat can be transferred to/from the material, not by the inherent martensitic transformation speed at the atomic-lattice scale (approaching the elastic shear wave speed). The boundary value problem may now have three time scales: one for the inherent kinetics (usually the shortest), one for thermal heat transfer, and one for any applied mechanical loading.

In the limit as $v_0 \to \infty$, the kinetic relation can be expressed as $(\mu \pm \mu_c)V = 0$ (see Fig. 10b). One must be careful with such a scheme, however, since the kinetic function is not defined for all values of μ, and there may be cases where the gradient of the chemical force exceeds the critical value for all admissible phase fractions. An alternative kinetic relation that may be numerically desirable is a non-linear relation, such as

$$V(\mu) = \begin{cases} -v_\infty[1 - e^{\lambda_v(\mu+\mu_c)}] & : \quad \mu < -\mu_c \\ 0 & : \quad -\mu_c \leqslant \mu \leqslant \mu_c \\ v_\infty[1 - e^{-\lambda_v(\mu-\mu_c)}] & : \quad \mu > \mu_c. \end{cases} \tag{54}$$

where v_∞ is the maximum possible transformation rate. This relation is initially stiff, but remains bounded to avoid infinite transformation rates (see Fig. 10c).

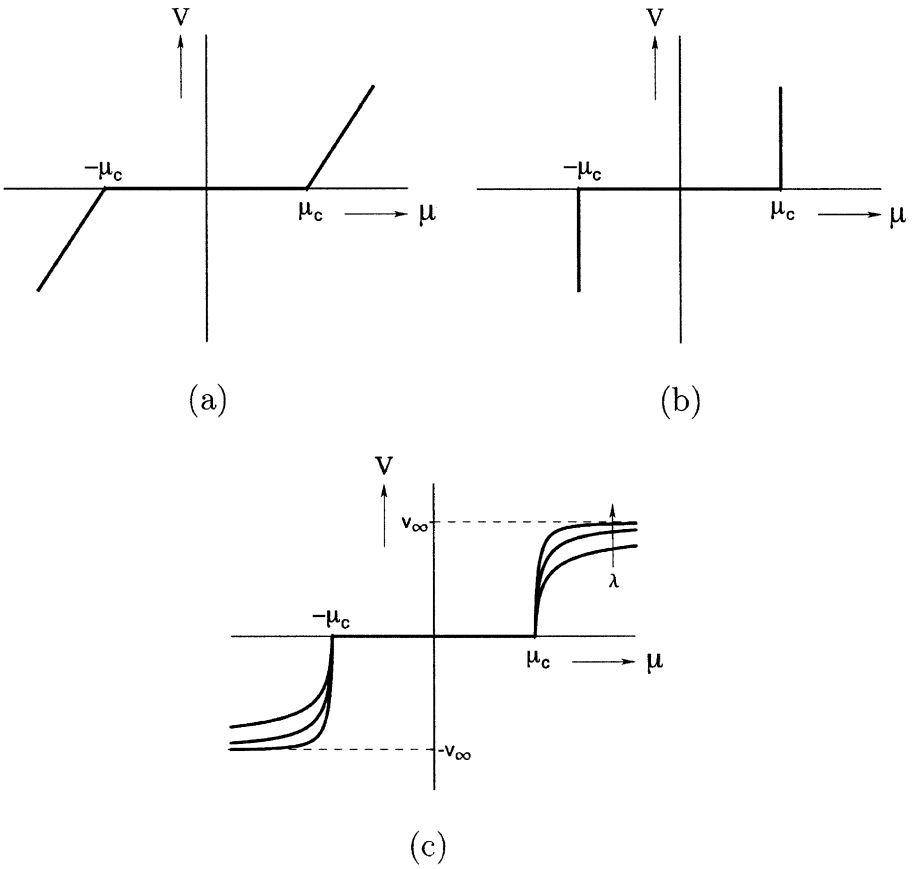

Fig. 10. Hysteretic kinetic relations: (a) linear relation, (b) infinite transformation speed, (c) non-linear, bounded transformation speed.

The above discussion applies for the interior of the admissible phase space. Some modification is required to satisfy Eq. (25) along phase space boundaries,

$$\xi_1 \geqslant 0, \quad \xi_2 \geqslant 0, \quad 1 - (\xi_1 + \xi_2) \geqslant 0. \tag{55}$$

One can devise a switching function to ensure the current phase fraction remains within the admissible region. The kinetic relation is now written as

$$\dot{\boldsymbol{\xi}} = V(\boldsymbol{\mu} \cdot \boldsymbol{v})\boldsymbol{v}, \tag{56}$$

where $\boldsymbol{v}$ is a unit vector that behaves (see Fig. 11) as

$$\boldsymbol{v} = \begin{cases} \boldsymbol{\mu}/\mu & : \quad \text{interior}, \quad \text{for all } d_j > 0 \\ \boldsymbol{t}^{(j)} & : \quad \text{on edge } j, \quad \text{for } d_j = 0, \ \ j = 1,2,3, \end{cases} \tag{57}$$

and the d_js are the distances to the three edges $\{\xi_2, 1 - (\xi_1 + \xi_2), \xi_1\}$ having tangent vectors $\boldsymbol{t}^{(j)}$. Note that $\dot{\boldsymbol{\xi}}$ may become discontinuous at the edges of $\boldsymbol{\xi}$-space, and some form of smoothing may be desirable for the numerical implementation.

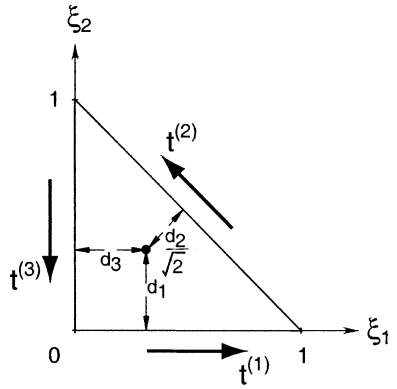

Fig. 11. Edge tangent vectors in the admissible phase space.

5. Demonstration of constitutive behavior

A specific constitutive model is now demonstrated for several imposed temperature and strain histories. In order to illustrate the material behavior for any single axial position X, we ignore (for the moment) any gradients of strain and temperature and treat strain and temperature as control parameters. The sample results that follow were implemented numerically in Mathematica (Wolfram Research, 1999). The kinetic relation was solved using a fifth order Cash–Karp procedure (a variant of the Runge–Kutta algorithm) with adaptive time stepping (Press et al., 1992). Switching functions were included to ensure phase fractions remain within the admissible phase region according to Eq. (57), and the non-linear kinetic relation (54) was implemented.

Table 1 gives values of material constants for a typical NiTi SMA. The table is divided into two columns to indicate which parameters are well known (and do not change much between different NiTi alloys) and which have been fitted for the particular alloy of Fig. 2. Fig. 12 shows a fit of the stress-induced transformations, $A \rightarrow M^+$ and $A \leftarrow M^+$, for the NiTi material of Fig. 2. The temperature scale is normalized by a reference temperature, θ_R, according to $\bar{\theta} \equiv (\theta - \theta_R)/\theta_R$, and the stress is normalized by the austenite modulus, $\overline{\Sigma} \equiv \Sigma/E_A$. The reference temperature suggested by the fit of Fig. 12 is 286 K. Note that this value is close to the average of the temperatures associated with the austenite and martensite latent heat peaks, 283 K (see Fig. 1). The slope of the transformation stresses, $d\overline{\Sigma}/d\bar{\theta}$, in Fig. 12 is 0.0316 (7.73 MPa/K), and the hysteresis stress, $\overline{\Sigma}_{hyst}$, is 0.0021 (147 MPa). The slope, $d\overline{\Sigma}/d\bar{\theta}$, predicted by the Clausius–Clapeyron relation is

$$\frac{d\overline{\Sigma}}{d\bar{\theta}} = \left(\frac{\Delta\bar{h}}{\Delta\varepsilon}\right)_{eqm}^{M^+ \rightarrow A}, \tag{58}$$

Table 1
Material constants

Known	Fitted
$\rho_0 = 6.5 \times 10^6$ g/m^3	$\beta = 0.05$
$E_A = 70$ GPa	$\theta_R = 286$ K
$E_M = 46.7$ GPa	$\mu_c = 1.077$ J/g
$c_0 = 0.5$ J/gK	$s_0 = 1$ J/gK

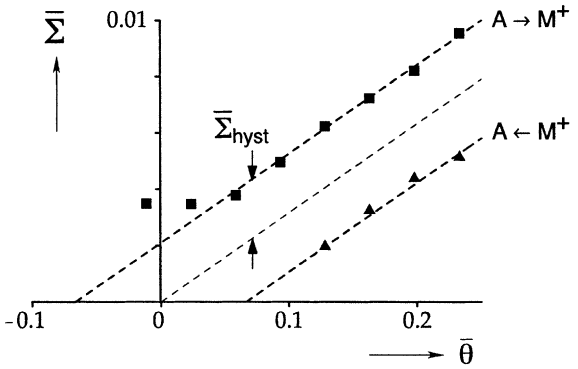

Fig. 12. Fit of propagation stresses for NiTi wire: $d\bar{\Sigma}/d\bar{\theta} = 0.0316$, $\bar{\Sigma}_{hyst} = 0.0021$, $\theta_R = 286$ K.

where $\bar{h} \equiv \rho_0 h/E_A$ is the normalized enthalpy. Using the measured (stress-free) enthalpy change of 15.6 J/g and transformation strain of about 0.05, the predicted value is $d\bar{\Sigma}/d\bar{\theta} = 0.029$, which is within 10% of the fitted value of 0.0316. It should be recognized that the stress-free enthalpy change may be different than the value under stress, but the stress dependent enthalpy change is difficult to measure in practice.

Specific temperature-dependent parameters $\varepsilon_n(\theta)$ and $E_t(\theta)$ are chosen as piecewise linear functions (see Table 2 and Fig. 13), separating the behavior into two regimes one on either side of the reference temperature, θ_R. The parameters $\varepsilon_n(\theta)$ and $E_t(\theta)$ are chosen according to the Maxwell construction to fit the average of the forward/reverse transformation stresses for temperatures above θ_R. Unfortunately, most experimental data on NiTi wire do not include nucleation stresses, since they are usually masked by the inevitable stress concentrations at the grips where the onset of transformation usually occurs. (However,

Table 2
Piecewise linear fit for temperature-dependent (non-dimensional) parameters

$\bar{\theta}$	ε_n	$\bar{E}_t$	$\bar{\phi}_{mix}$
−0.2	−0.00521	0.0117	−0.000279
0	0	0.0117	0
0.2	0.00734	−0.0283	0.000279

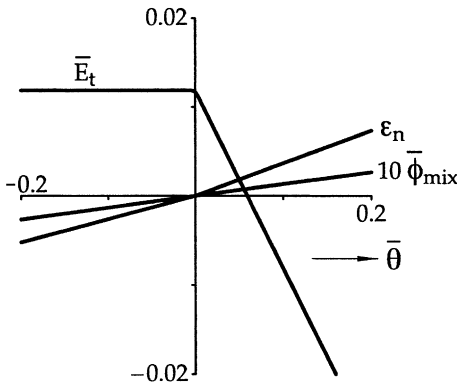

Fig. 13. Temperature-dependent functions for ε_n, $\bar{E}_t$, and $\bar{\phi}_{mix}$.

small nucleation valleys can sometimes be observed during the reverse transformation upon unloading.) One exception is Shaw and Kyriakides (1997) where nucleation stresses were measured for a somewhat different NiTi material using dogbone specimens machined from thin strips. An experimental method is also under development in the author's laboratory to measure the nucleation peaks in wire specimens through the use of non-uniform temperature fields (see Iadicola and Shaw, 2000). Values of the nucleation strains are estimated (see Table 2) for the NiTi material of Fig. 2 based on the author's experience with ongoing experiments on other similar NiTi wire samples. In general, for temperatures above $\theta_R(\bar{\theta} > 0)$ the nucleation peaks become larger as the temperature increases, meaning that $(d\varepsilon_n/d\theta)^{A\to M^+}$ is a rate somewhat greater than $(d\overline{\Sigma}/d\theta)^{A\to M^+}$, and therefore, $dE_t/d\theta$ is negative. At temperatures below $\theta_R(\bar{\theta} < 0)$ the parameters ε_n and E_t loose their direct interpretation. It is known that the material response is much less temperature sensitive at temperatures below θ_R than for temperatures above θ_R. A constant value of E_t and a linear ε_n curve with a reduced slope were found to produce reasonable behavior at low temperatures. The parameter, $\phi_{mix}(\theta)$, was chosen to be linear with a positive slope across the entire temperature range, passing through zero at the reference temperature $(\bar{\theta} = 0)$. Under stress free conditions it causes the free energy to favor twinned martensite $(\xi_1 = \xi_2 = \frac{1}{2})$ at low temperatures and austenite $(\xi_1 = \xi_2 = 0)$ at high temperatures.

Isothermal mechanical responses are now shown in which the strain history is imposed in load–unload segments under tension $(\varepsilon > 0)$, then compression $(\varepsilon < 0)$ as shown in Fig. 14. The time for each leg of the strain history is normalized to unity according to $\bar{t} = t/\tau$, where τ is the characteristic time for loading. An isothermal response is shown in Fig. 15 for a relatively high temperature ($\bar{\theta} = 0.1979$, or 70 °C). Strain gradients are prescribed to be zero. The figure shows the predicted homogeneous stress–strain response, the rate of heat change in the material, the change in the phase fractions with strain, and the trajectories in the phase fraction space. During each load segment, Fig. 15a shows a trilinear mechanical behavior with an unstable intermediate transformation branch. An experimental response is overlaid for comparison, but one must recognize that it represents the force–displacement behavior arising from the inhomogeneous response and propagating phase fronts. Each load and unload plateau stress in the experimental response can be interpreted as the Maxwell stress for the hysteretic non-monotonic homogeneous behavior shown. Fig. 15b shows the predicted latent heat changes according to Eq. (32), non-dimensionalized by $d\overline{Q}/d\bar{t} \equiv \rho_0 \tau \dot{Q}_s/E_A$, that are necessary to maintain an isothermal temperature. As expected, the heat changes under tension are exothermic (negative) during loading ($A \to M^+$) and endothermic (positive) during unloading ($A \leftarrow M^+$). The compressive mechanical response shown is symmetric to the tensile response and the heat changes follow the same exothermic/endothermic response during loading/unloading. The changes in phase fractions (ξ_1, ξ_2) are shown in Fig. 15c and d. Fig. 15c shows the changes as a function

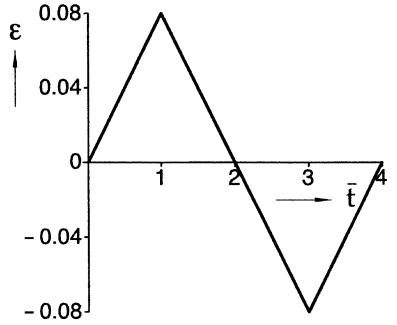

Fig. 14. Imposed strain history for isotherms.

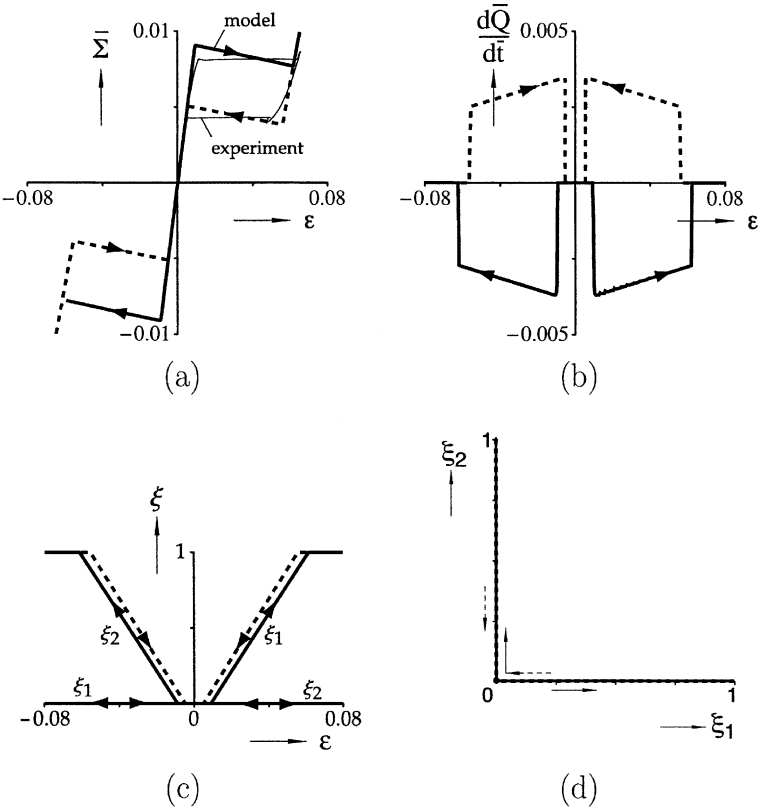

Fig. 15. Isothermal response at $\bar{\theta} = 0.1979$ (70 °C): (a) stress–strain isotherm, (b) heat changes, (c) phase fraction changes, (d) phase space trajectory.

of the imposed strain and Fig. 15d shows the trajectories in ξ_1–ξ_2 space. During tensile loading, the M^- fraction remains zero while M^+ changes hysteretically, and vice versa during compressive loading.

Fig. 16 shows the tensile, then compressive responses, for the case starting with twinned martensite ($\xi_1 = \xi_2 = \frac{1}{2}$) at a relatively low temperature, ($\bar{\theta} = -0.0115$, or 10 °C). Fig. 16a shows the mechanical response where a reversal of stress is now necessary to reverse the direction of phase transformation. It shows the correct behavior (ferroelectric-like response) with positive tangent modulus (stable behavior) for twinning/detwinning of martensite. However, the mechanical hysteresis is underpredicted compared to the experiment. This is likely a result of the simplifying assumption that the critical chemical driving force μ_c is constant. It may, in fact, be a function of the phase fraction or temperature or even the direction of phase transformation. Nevertheless, the response is a reasonable qualitative representation of detwinning ($M^+/M^- \rightarrow M^+$). Fig. 16b shows minimal heat changes as expected. Fig. 16c and d show the phase fraction histories and trajectories, respectively. The austenite phase fraction ($1 - \xi_1 - \xi_2$) remains zero and the phase state changes from twinned martensite (M^+/M^-) to detwinned martensite (M^+) under tension, then to detwinned martensite (M^-) under compression.

An interesting predicted response occurs at the intermediate temperature of $\bar{\theta} = 0.02339$, or 20 °C, starting in the austenite phase as shown in Fig. 17. During loading, a stable transformation occurs from A to M^+ as shown in Fig. 17a and b, but then during unloading the phase fraction trajectory proceeds towards a mixture of A, M^+, and M^-. Continued loading into compression is shown in Fig. 17c and d. The

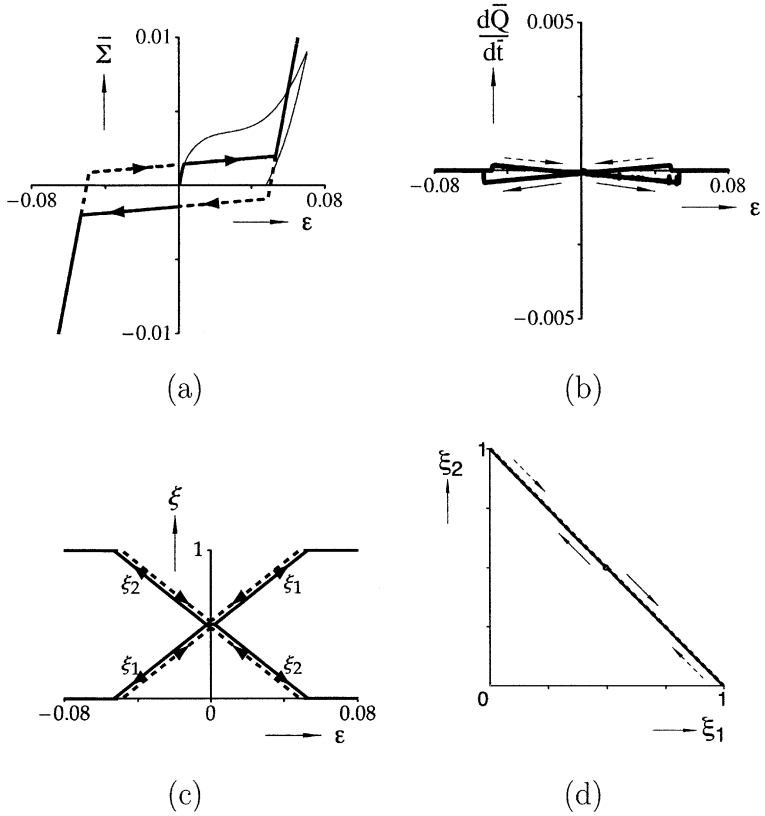

Fig. 16. Isothermal response at $\bar{\theta} = -0.0115$ (10 °C): (a) stress–strain isotherm, (b) heat changes, (c) phase fraction changes, (d) phase space trajectory.

mechanical response exhibits an interesting 'staircase' history and the phase trajectory traces a 'bow-tie' shape in ξ_1–ξ_2 phase space. The step in the mechanical response of Fig. 17c occurs when the phase fraction reaches a boundary in ξ_1–ξ_2 space and the trajectory suddenly changes direction (Fig. 17d). The hysteresis is less during angled transformation paths than when phase transformation occurs along horizontal ($\xi_2 = 0$) or vertical ($\xi_1 = 0$) boundaries. This is a feature of the model again due to the assumed constant μ_c that may warrant future modeling improvement.

Fig. 18 shows a series of the predicted mechanical isotherms for tensile loading/unloading at several temperatures overlaid with the results of NiTi force–displacement experiments. While details of some of the non-linearities in the experiments are missing, the calculated constitutive behavior successfully captures the overall trends.

Lastly, calorimetry results are simulated. Fig. 19a shows the predicted heat changes and Fig. 19b and c show the transformation paths for the case of zero applied strain (also zero stress) and prescribed temperature ramps. A hysteresis is calculated that is similar to the M_s and A_s temperatures measured in Fig. 1. (No R-phase is included in the model.) The calculated response differs in that the latent heat peaks are quite narrow (actually approach delta functions as the temperature rate becomes slow). The model does not as yet capture the athermal nature of the transformation in NiTi. Fig. 20 shows a similar result for the case of a fixed applied strain, $\varepsilon = 0.005$. Fig. 20a shows the predicted calorimetry, Fig. 20b shows the predicted stress response, and Fig. 20c and d show the transformation paths. As expected, the calorimetry is similar to

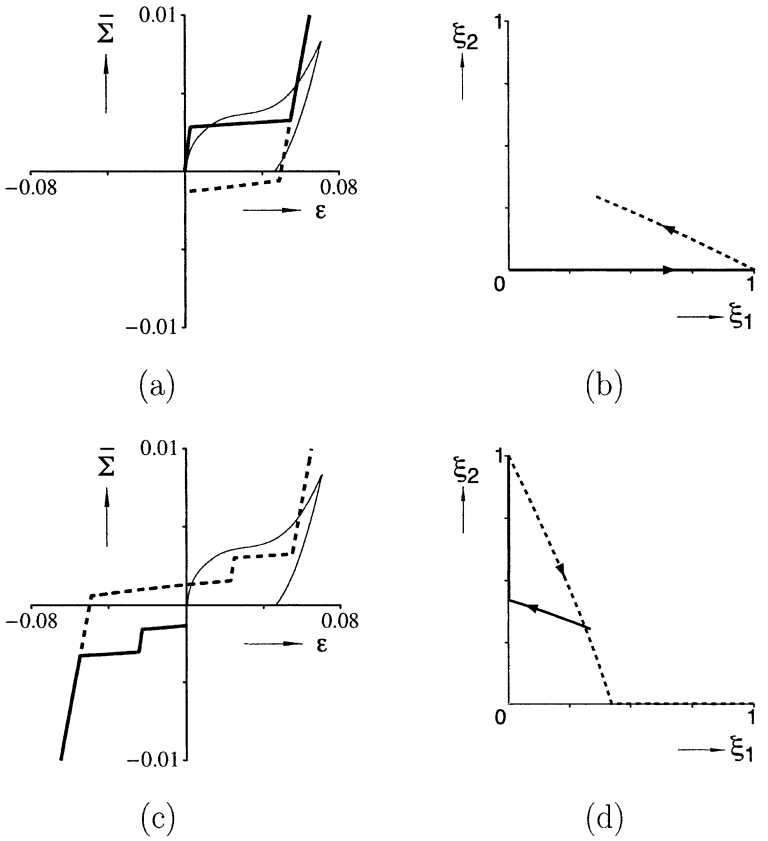

Fig. 17. Isothermal response at $\bar{\theta} = 0.02339$ (20 °C): (a) tensile stress–strain isotherm (initially A), (b) tensile phase space trajectory, (c) compressive stress–strain isotherm, (d) compressive phase space trajectory.

the previous case, but the stress undergoes a hysteretic loop and the M^+ phase is somewhat favored at the expense of the M^- phase.

6. An example numerical problem

A simplified problem is demonstrated in this section in order to exhibit the ability to model propagating phase boundaries. The 1-D wire of interest is under isothermal conditions at a pseudoelastic temperature, stretched under displacement control at constant rate. This represents the case where the displacement rate is sufficiently slow that the ambient medium can extract or supply heat, as necessary, to keep the temperature field constant. As seen in experiments at very slow loading rates (Shaw and Kyriakides, 1995) only a single transformation front occurs in the specimen, starting from one end at the site most favourable to initiate phase transformation (geometric imperfection or stress concentration) and traversing the wire length to the other end. In this case the heat equation can be ignored, since the temperature remains constant. At an elevated (pseudoelastic) temperature only one internal parameter for M^+ (ξ_1) is active, since M^- does not appear.

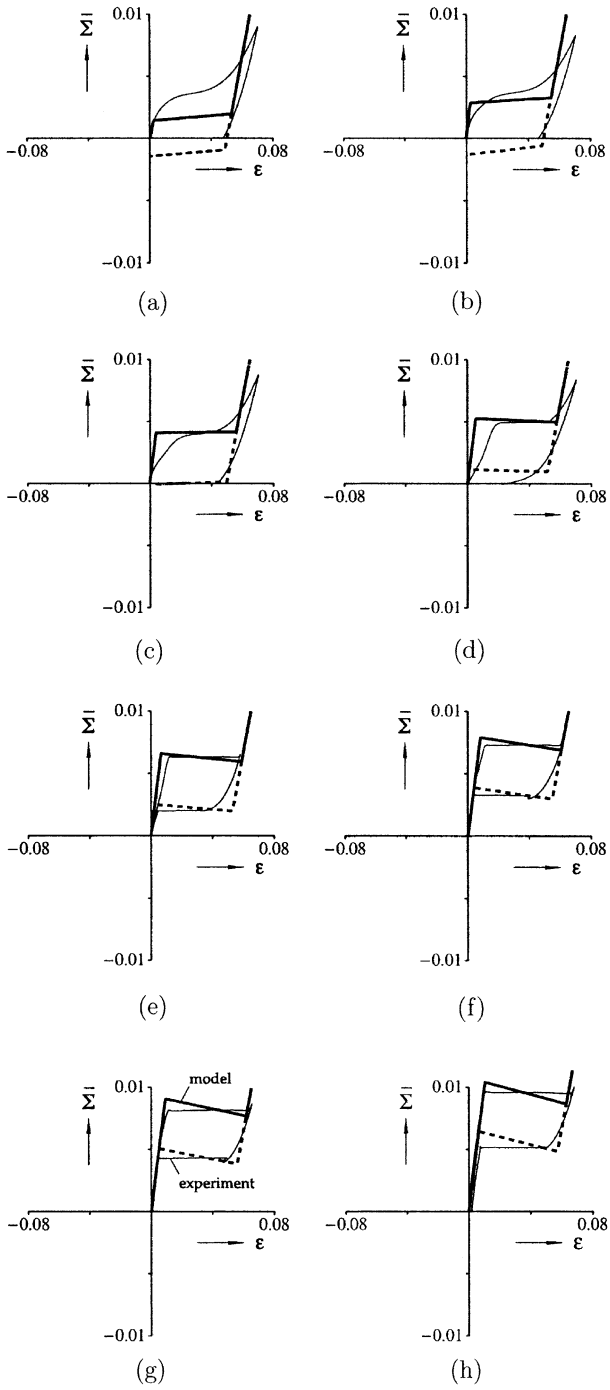

Fig. 18. Pointwise stress–strain isotherms and force–displacement experiments at $\bar{\theta}$s: (a) −0.01152 (initially M^+/M^-), (b) 0.02339 (initially A), (c) 0.05830, (d) 0.09321, (e) 0.1281, (f) 0.1630, (g) 0.1979, (h) 0.2328.

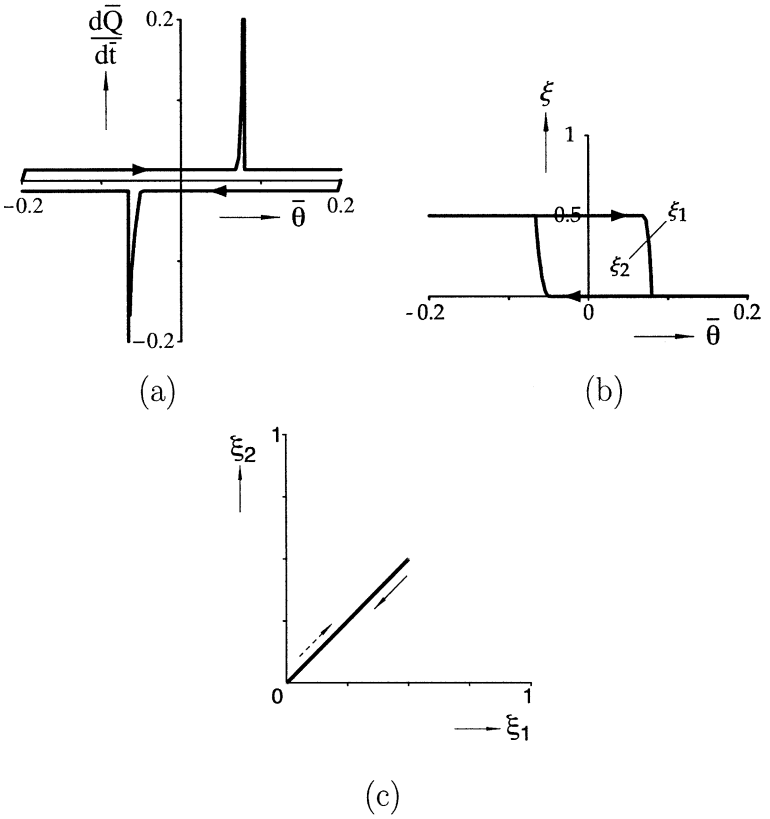

Fig. 19. Temperature controlled response at zero strain: (a) calorimetry, (b) phase fraction changes, (c) phase space trajectories.

The initial conditions for $u(X,t)$ are

$$u(X,0) = \dot{u}(X,0) = 0, \quad \text{for } 0 \leqslant X \leqslant L \tag{59}$$

and the boundary conditions are

$$u(0,t) = u'(0,t) = u'(L,t) = 0, \quad u(L,t) = \delta(t), \quad \text{for} \quad t > 0, \tag{60}$$

where the displacement is imposed according to a load–unload ramp with an average strain rate of $\dot{\delta}/L = 1 \times 10^{-1}\ \mathrm{s}^{-1}$. Actually, the strain rate is relatively unimportant since there are no thermal effects, but it sets the loading time scale (1 s for a ramp to 0.1 average strain) to be compared to the characteristic time of the kinetic law.

$$\delta(t) = \begin{cases} \dot{\delta}t & : \quad \text{for } 0 \leqslant t \leqslant \tau \\ \dot{\delta}(\tau - t) & : \quad \text{for } \tau < t \leqslant 2\tau, \end{cases} \tag{61}$$

The equilibrium equation is solved numerically with a finite element research code (SARPP, 2001). The axial length is discretized by 100 equal-length finite elements. Each finite element has two nodes with two degrees of freedom (u, u') per node. This ensures continuity of displacement and strain across interelement nodes. The displacement field is interpolated with cubic Hermite polynomials. An area imperfection of 1% at $X = 0$, decreasing linearly to zero at the other end, is introduced to model the effect of a stress concentration at one of the grips. It is introduced to control the location of the initial nucleation.

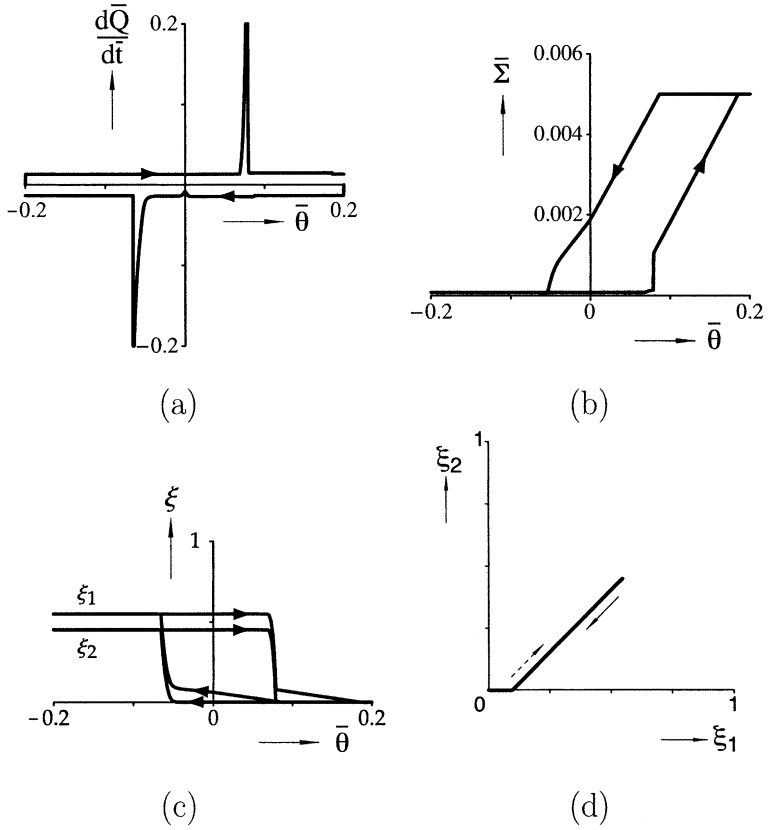

Fig. 20. Temperature controlled response at fixed strain of 0.005: (a) calorimetry, (b) stress response, (c) phase fraction changes, (d) phase space trajectory.

Parameters used in the finite element simulations are given in Table 3. The linear kinetic law of equation (53) is used. As previously mentioned a bar over a variable denotes a non-dimensional parameter. Non-dimensional parameters for the strain gradient coefficient, the critical chemical potential, and the linear kinetic law coefficient are defined as $\bar{\gamma} \equiv \gamma/(E_A L^2)$, $\bar{\mu}_c \equiv \mu_c \rho_0/E_A$, $\bar{v}_0 \equiv v_0 E_A \tau/\rho_0$, respectively. The critical chemical potential, $\bar{\mu}_c$, is chosen as before to model the known hysteresis in the pseudoelastic loops. The kinetic coefficient, $\bar{v}_0$, is chosen to give a very short relaxation time compared to the characteristic loading time, τ.

Table 3
Parameters used in example finite element simulations (Fig. 21)

$\bar{\theta} = 0.1979$
$\overline{\Delta E} = -0.333$
$\beta = 0.05$
$\varepsilon_n = 0.00726$
$\overline{E}_t = -0.0279$
$\bar{\gamma} = 2 \times 10^{-4}, 5 \times 10^{-4}$
$\bar{\mu}_c = 1 \times 10^{-4}$
$\bar{v}_0 = 2 \times 10^{6}$

Under end-displacement control, inertia effects can be avoided by using a rather strong strain gradient coefficient (γ) and relatively large imperfection, so that equilibrium paths during nucleation events occur without a cusp in the force–displacement response. Since the length scale associated with the gradient effect is of the order of the wire diameter, a large gradient coefficient corresponds to the case of a short segment of wire (say, $L/D < 5$). This is a simplification of the behavior in experiments on long wires (say, $L/D > 100$), where such cusps do exist and nucleation events are dynamic (a subjects for later study).

Fig. 21 presents the results of finite element simulations for two different values of the strain gradient coefficient ($\bar{\gamma}$). Fig. 21a shows the case with the smaller value of $\bar{\gamma}$. The calculated force–displacement ($\overline{\Sigma} - \delta/L$) shows an initial austenite elastic branch during stretching at a constant end-displacement rate. A critical load is reached and transformation to M^+ begins at the end $X = 0$ as seen in the loading profiles of ξ_1 near $\delta/L = 0.01$. As nucleation of M^+ continues at $X = 0$ (see the loading profile for $\delta/L = 0.015$) the load drops somewhat. Soon thereafter a fully formed transformation front is established and it propagates to the right (as seen in the loading profiles). This occurs at constant load until the front nears the right end ($X/L = 1$). The front disappears in a sort of reverse nucleation and there is a further momentary drop in load near $\delta/L = 0.06$. This sequence during transformation of an initial nucleation peak, a load plateau, then a slight drop during coalescence at the end of transformation have been observed in carefully controlled experiments (Shaw and Kyriakides, 1997). Continued stretching occurs in a relatively uniform manner, and the load rises along the elastic branch associated with 100% M^+.

The end-displacement direction is then reversed and the material is gradually unloaded. Unloading occurs elastically along the M^+ elastic branch until a reverse transformation is initiated at $X/L = 1$ some time after the end-displacement decreases below $\delta/L = 0.055$. A reverse nucleation event occurs and an upside-down nucleation peak (valley) is seen in the force–displacement response. A single front propagates from right to left as seen in the profiles of M^+ during unloading. The reverse transformation is complete once the end-displacement decreases below $\delta/L = 0.005$, and a slight upturn in the force–displacement response is seen then. Again, the reverse transformation exhibits details which have been observed in experiments. The remainder of the unloading occurs elastically and the pseudoelastic cycle is complete when the end-displacement reaches zero.

Fig. 21b shows the results of a finite element simulation for a value of the strain gradient coefficient ($\bar{\gamma}$) 10 times larger than before. The calculated response is quite similar to the previous case, except that nucleation and coalescent events occur more gradually, and the profiles of M^+ phase fraction are broader in length. In this way the strain gradient coefficient can be tuned to the particular wire geometry being used. Since the strain gradient energy is $\frac{\gamma}{2}\varepsilon'^2$, a simple dimensional analysis shows that the profile length of a transformation front ($\Delta L_\xi/L$) is roughly proportional to $\sqrt{\bar{\gamma}}$.

Further numerical simulations of the fully coupled thermomechanical problem derived in this paper and a thorough parametric study are left for later work. The role of axial heat transfer versus radial heat transfer, for example, is an interesting issue, which has been studied experimentally in Shaw and Kyriakides (1995, 1997) and numerically in Iadicola and Shaw (in preparation). The current approach should be able to address these issues in a more computationally efficient way.

7. Summary and conclusions

A coupled thermomechanical boundary value problem and constitutive relations were derived for a 1-D SMA element. Mechanical equilibrium and heat equation were derived with strain gradient effects. Constitutive relations were derived consistent with fundamental thermodynamic considerations and experimental observations of typical SMA wires. An explicit Helmholtz free energy function was developed that included internal field variables representing phase fractions of austenite and 1-D variants of martensite. It

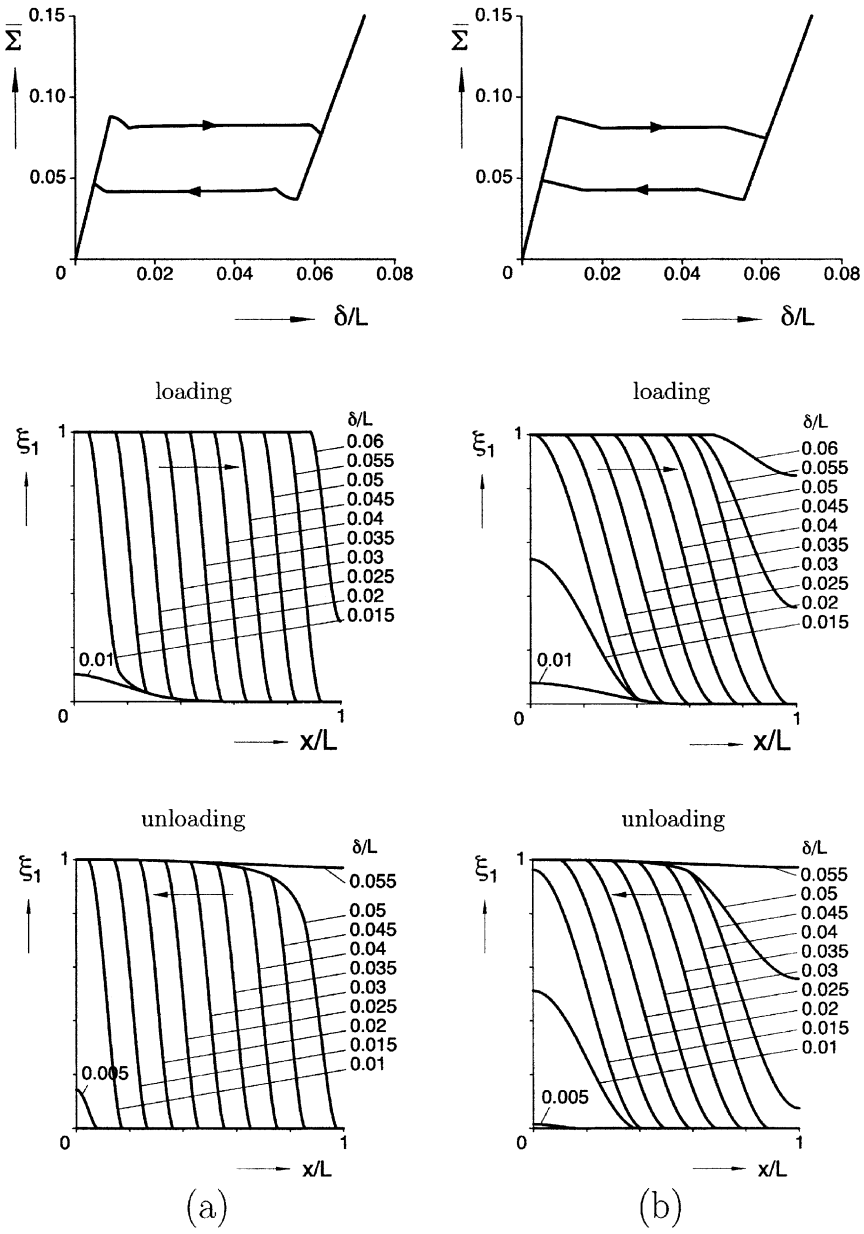

Fig. 21. Results of two finite element simulations (force–displacement response and profiles of M^+ fraction for loading and unloading) for isothermal ($\bar{\theta} = 0.1979$) pseudoelastic behavior ($A \leftrightarrow M^+$) under an end-displacement (δ/L) controlled cycle: (a) $\bar{\gamma} = 5 \times 10^{-5}$, (b) $\bar{\gamma} = 5 \times 10^{-4}$.

was calibrated to experimental mechanical isotherms and differential scanning calorimetry of a commercially available NiTi SMA. The free energy was augmented by a hysteretic kinetic relation that governs the rate of phase transformation as a function of chemical driving forces. Strain-controlled and temperature-controlled responses were demonstrated for a typical NiTi material under homogenous strain and tem-

perature conditions, and an isothermal pseudoelastic response with a single transformation front was demonstrated using finite element analysis.

Overall, the model provides a satisfactory representation of the uniaxial thermomechanical behavior of an SMA wire. It provides a thermodynamically consistent approach to model the shape memory effect, the pseudoelastic behavior, along with latent heat changes and possible unstable transformation behavior. It is an attempt to capture all these phenomena in a single model. The agreement with experiments is reasonable, capturing the basic trends. Future refinement to capture certain details of the non-linear mechanical behavior, the athermal nature of calorimetry, and low temperature mechanical hysteresis are certainly possible.

A key parameter of the model is a user-specified tangent modulus for stress-induced transformation that can be used to trigger unstable behavior. The model is appropriate for finite element implementation, since the inclusion of strain gradient effects avoids singularity of the equilibrium equation during the transition from stable to unstable mechanical behavior. There is no need to explicitly track propagating phase boundaries as discontinuous quantities, since these will arise naturally as smooth, localized propagating fields in the boundary value problem. The inclusion of strain gradient effects allows one to model the finite extent of nucleation events and transformation fronts, which can in turn determine the non-uniform temperature field and the number of nucleations and ensuing fronts that exist during transformations. Consequently, the model should be suitable to numerically study a variety of interesting future applications, such as SMA wires with propagating transition fronts embedded in interacting fluid or solid media.

Acknowledgements

The author would like to sincerely thank Yves Leroy for his assistance with the finite element implementation and Nicolas Triantafyllidis for helpful discussions. The financial support of the National Science Foundation (CAREER grant) and the University of Michigan (Rackham Fellowhip) is gratefully acknowledged.

References

Abeyaratne, R., Knowles, J.K., 1993. A continuum model of a thermoelastic solid capable of undergoing phase transitions. Journal of the Mechanics and Physics of Solids 41, 541–571.

Abeyaratne, R., Chu, C., James, R.D., 1996. Kinetics of materials with wiggly energies: Theory and application to the evolution of twinning microstructures in a cu-al-ni shape memory alloy. Philosophical Magazine A 73 (2), 457–497.

Ball, J.M., James, R.D., 1987. Fine phase mixtures as minimizers of energy. Archive for Rational Mechanics and Analysis 100, 13–52.

Batthacharya, K., Kohn, R.V., 1996. Symmetry, texture and the recoverable strain of shape memory polycrystals. Acta Metallurgica et Materialia 44, 529–542.

Boyd, J., Lagoudas, D., 1994. A constitutive model for simultaneous transformation and reorientation in shape memory materials. Mechanics of Phase Transformations and Shape Memory Alloys, AMD 189, 159–177.

Brinson, L.C., 1993. One dimensional constitutive behavior of shape memory alloys: thermomechanical derivation with non-constant material functions. Journal of Intelligent Material Systems and Structures 4, 229–242.

Buehler, W.J., Gilfrich, J.V., Wiley, R.C., 1963. Effect of low-temperature phase changes on the mechanical properties of alloys near composition TiNi. Journal of Applied Physics 34, 1475–1477.

Coleman, B.D., Gurtin, M.E., 1967. Thermodynamics with internal state variables. The Journal of Chemical Physics 47 (2), 597–613.

Coleman, B.D., Noll, W., 1963. The thermodynamics of elastic materials with heat conduction and viscosity. The Archives of Rational Mechanics and Analysis 13 (1), 167–178.

Coleman, B.D., 1983. Necking and drawing in polymeric fibers under tension. The Archives of Rational Mechanics and Analysis 83, 115–137.

Duerig, T.W., Melton, K.N., Stöckel, D., Wayman, C.M. (Eds.), 1990. Engineering Aspects of Shape Memory Alloys. Butterworth–Heinemann, London.

Elliott, R., Shaw, J., Triantafyllidis, N. (accepted). Stability of thermally-induced martensitic transformation in bi-atomic lattices. Journal of the Mechanics and Physics of Solids.

Faulkner, M.G., Amalraj, J.J., Bhattacharyya, A., 2000. Experimental determination of thermal and electrical properties of Ni-Ti shape memory wires. Smart Materials and Structures 9, 632–639.

Fleck, N.A., Hutchinson, J.W., 1996. In: Hutchinson, J.W., Wu, T.Y., (Eds.), Strain Gradient Plasticity, Advances in Applied Mechanics, vol. 33. Academic Press, New York.

Gall, K., Sehitoglu, H., Chumlyakov, Y., Kireeva, I., 1999. Tension-compression asymmetry of the stress-strain response in aged single crystal and polycrystalline NiTi. Acta Materialia 47 (4), 1203–1217.

Iadicola, M.A., Shaw, J.A., 2000. An experimental setup for measuring unstable thermo–mechanical behavior of a shape memory alloy wire. Proceedings of the Adaptive Structures and Material Systems Symposium, ASME International Mechanical Engineering Congress and Exposition, Orlando, FL, 19–24.

Iadicola, M.A., Shaw, J.A. (in preparation) Rate and thermal sensitivities of material instabilities in a shape memory alloy. International Journal of Plasticity.

Incropera, F.P., DeWitt, D.P., 1996. Introduction to Heat Transfer, third ed. Wiley, New York.

Knowles, J.K., 1999. Stress-induced phase transitions in elastic solids. Computational Mechanics 22, 429–436.

Leo, P.H., Shield, T.W., Bruno, O.P., 1993. Transient heat transfer effects on the pseudoelastic behavior of shape-memory wires. Acta Metallurgica et Materialia 41, 2477–2485.

Leroy, Y., Molinari, A., 1993. Spatial patterns and size effects in shear zones: A hyperelastic model with higher–order gradients. Journal of the Mechanics and Physics of Solids 41 (4), 631–663.

Levitas, V.I., 1994. Thermomechanical description of pseudoelasticity—the threshold-type dissipative force with discrete memory. Mechanics Research Communications 21 (3), 273–280.

Liu, Y., Liu, Y., Van Humbeeck, J., 1998. Lüders-like deformation associated with martensite reorientation in NiTi. Scripta Materialia 39 (8), 1047–1055.

Mindlin, R.D., 1965. Second gradient of strain and surface–tension in linear elasticity. International Journal of Solids and Structures 1, 417–438.

Ngan, S.-C., Truskinovsky, L., 1999. Thermal trapping and kinetics of martensitic phase boundaries. Journal of the Mechanics and Physics of Solids 1, 141–172.

Otsuka, K., Wayman, C.M. (Eds.), 1998. Shape Memory Materials. Cambridge University Press, Cambridge.

Otsuka, K., Sawamura, T., Shimizu, K., 1971. Crystal structure and internal defects of equiatomic TiNi martensite. Physical State Solid (A) 5, 457.

Patoor, E., Eberhardt, A., Berveiller, M., 1995. Micromechanical modeling of the superelastic behavior. Journal de Physique IV 5 (C2), 501.

Press, W.H., Teukolsky, S.A., Vetterling, W.T., Flannery, B.P., 1992. Numerical Recipes in C, The Art of Scientific Computing, second ed. Cambridge University Press, Cambridge.

SARPP, User Manual, École Polytechnique (LMS) and the University of Michigan (Aerospace Engineering), 2.0 edition, 2001.

Shaw, J.A., Kyriakides, S., 1995. Thermomechanical aspects of NiTi. Journal of the Mechanics and Physics of Solids 43 (8), 1243–1281.

Shaw, J.A., Kyriakides, S., 1997. On the nucleation and propagation of phase transformation fronts in a NiTi alloy. Acta Materialia 45 (2), 673–700.

Shaw, J.A., Kyriakides, S., 1998. Initiation and propagation of localized deformation in elastoplastic strips under uniaxial tension. International Journal of Plasticity 43 (10), 837–871.

Shaw, J.A., 1997. Material Instabilities in a Nickel-Titanium Shape Memory Alloy. PhD dissertation, Department of Aerospace Engineering, The University of Texas at Austin.

Shaw, J.A., 2000. Thermo-mechanical simulations of localized thermo–mechanical behavior in a NiTi shape memory alloy. International Journal of Plasticity 46 (5), 541–562.

Siredey, N., Patoor, E., Berveiller, M., Eberhardt, A., 1999. Constitutive equations for polycrystalline thermoelastic shape memory alloys. part I. intragranular interactions and behavior of the grain. International Journal of Solids and Structures 36, 4289–4315.

Sittner, P., Takakura, M., Tokuda, M., 1995. The stabilization of transformation pathway in stress induced martensite. Scripta Metallurgica et Materialia 32 (12), 2073–2079.

Sun, Q.P., Hwang, K.C., 1993. Micromechanics modelling for the constitutive behavior of polycrystalline shape memory alloys—I derivation of general relations. Journal of the Mechanics and Physics of Solids 41 (1), 1–17.

Sun, Q.P., Zhong, Z., 2000. An inclusion theory for the propagation of martensite band in NiTi shape memory alloy wires under tensions. International Journal of Plasticity 16, 1169–1187.

Sun, Q.P., Li, Z.Q., Tse, K.K., 2000. On superelastic deformation of NiTi shape memory alloy micro–tubes and wires–band nucleation and propagation. Proceedings of IUTAM Symposium on Smart Structures and Structronic Systems, Magdeburg Germany, September 26–29.

Tanaka, K., Kobayashi, S., Sato, Y., 1986. Thermomechanics of transformation pseudoelasticity and shape memory effects in alloys. International Journal of Plasticity 2, 59–72.

Triantafyllidis, N., Bardenhagen, S., 1993. On higher order gradient continuum theories in 1-D nonlinear elasticity, derivation from and comparison to the corresponding discrete models. Journal of Elasticity 33, 259–293.

Truskinovsky, L., Zanzotto, G., 1996. Ericksen's bar revisited: Energy wiggles. Journal of the Mechanics and Physics of Solids 44 (8), 1371–1408.

Truskinovsky, L., 1993. Kinks versus shocks. Shock Induced Transitions and Phase Structures in General Media, IMA 52, 185–229.

Vainchtein, A., 1999. Dynamics of phase transitions and hysteresis in a viscoelastic ericksen's bar on an elastic foundation. Journal of Elasticity 57, 243–280.

Wolfram Research, Mathematica, fourth ed., 1999.

Zhang, X., Sun, Q.P., Yu, S., 2000. A non–invariant plane model for the interface in CuAlNi single crystal shape memory alloys. Journal of the Mechanics and Physics of Solids 48, 2163–2182.